

Fourier Series Expansion Based Filter Parametrization for Equivariant Convolutions

Qi Xie, Qian Zhao, Zongben Xu and Deyu Meng

Abstract—It has been shown that equivariant convolution is very helpful for many types of computer vision tasks. Recently, the 2D filter parametrization technique plays an important role when designing equivariant convolutions, and has achieved success in making use of rotation symmetry of images. However, the current filter parametrization method still has its evident drawbacks, where the most critical one lies in the accuracy problem of filter representation. Against this issue, in this paper we modify the classical Fourier series expansion for 2D filters, and propose a new set of atomic basis functions for filter parametrization. The proposed filter parametrization method not only finely represents 2D filters with zero error when the filter is not rotated (similar as the classical Fourier series expansion), but also substantially alleviates the fence-effect-caused quality degradation when the filter is rotated (which usually arises in classical Fourier series expansion method). Accordingly, we construct a new equivariant convolution method based on the proposed filter parametrization method, named F-Conv. We prove that the equivariance of the proposed F-Conv is exact in the continuous domain, which becomes approximate only after discretization. Moreover, we provide theoretical error analysis for the case when the equivariance is approximate, showing that the approximation error is related to the mesh size and filter size. Extensive experiments show the superiority of the proposed method. Particularly, we adopt rotation equivariant convolution methods to a typical low-level image processing task, image super-resolution. It can be substantiated that the proposed F-Conv based method evidently outperforms classical convolution based methods, while previous filter parametrization based equivariant convolutions fail to achieve satisfactory results. Specifically, this should be the first filter parametrization based equivariant convolution method performable on low-level image processing tasks, reflecting its intrinsic capability of faithfully preserving rotation symmetries in local image features.

Index Terms—Filter parametrization, equivariant convolution, Fourier series expansion, rotation symmetry of deep network, convolutional neural networks, image super-resolution.

1 INTRODUCTION

IN many computer vision and image processing tasks, there are usually kinds of transformation symmetries existing across both the local features and global semantic representations of images [1]. Typical examples include translation, rotation and reflection symmetries, intrinsically contained by objective images for both low-level and high-level computer vision tasks. It is desirable to make use of such transformation symmetries to reduce the number of model parameters as well as enhance the generalization capability of machine learning methods. In the past few years, convolutional neural network (CNN) based models have achieved great success in many fields of computer vision and image processing tasks, such as image recognition, object detection, semantic segmentation and image reconstruction [2]. One of the most principal reasons is that CNN is a shift equivariant network. That is, shifting an input image of CNN is equivalent to shifting all of its intermediate feature maps and output image. In other words, the translation symmetry is preserved through the entire CNN layers. Compared with conventional fully-connected neural networks, this translational equivariance property brings in weight sharing for CNN, makes the network parameters being used more efficiently, and thus leads to substantially better generalization capability. Recently, several kinds of equivariant CNNs have been further proposed to preserve rotations and reflection symmetries beyond current CNNs.

Qi Xie, Qian Zhao, Zongben Xu and Deyu Meng (corresponding author) are with School of Mathematics and Statistics, Xi'an Jiaotong University, Shaanxi, P.R.China, and Pazhou Lab, Guangzhou, P.R. China.
Email: {xie.qi, timmy.zhaqian, zbxu, dymeng}@mail.xjtu.edu.cn

It has been shown that equivariant CNNs can be very helpful for computer vision tasks on images like biomedical microscopy and astronomical images [3], [4], [5].

The early equivariant CNNs achieve $\pi/2$ degree rotations and reflection equivariant (i.e. $p4$ and $p4m$ group equivariant) on square lattices [6]. This kind of CNNs is designed based on the property that $\pi/2$ degree rotation and reflection on square lattice can be easily implemented by changing the position of elements in a convolutional filter, and element-shared filter can be easily designed in this way. Afterwards, HexaConv [7] expanded rotation equivariant to $\pi/3$ degree rotations (i.e., $p6$ and $p6m$ group equivariant) by replacing the commonly used square lattices with hexagonal lattices. However, this category of methods can only deal with a 4-fold or 6-fold rotational symmetry for images, since the practically used image data are mostly stored with square lattices and it is hard to be transformed into lattices other than hexagonal one.

Very recently, the filter parametrization technique has been employed to make use of more rotation symmetry in CNNs [3], [4], [5]. In 2018, Weiler et al. [3] proposed harmonics based steerable filters to achieve equivariance on arbitrary degree rotation in the continuous domain. Later on, Shen et al. [5] further proposed partial differential operator based equivariant convolution (PDO-eConv), where the theoretical error analysis is firstly provided when the equivariance is approximated in the discrete domain. The basic idea of these methods is to define the to-be-learnt filters as the linear combination of a set of basis functions (i.e., elementary filters) and learn the combination coeffi-

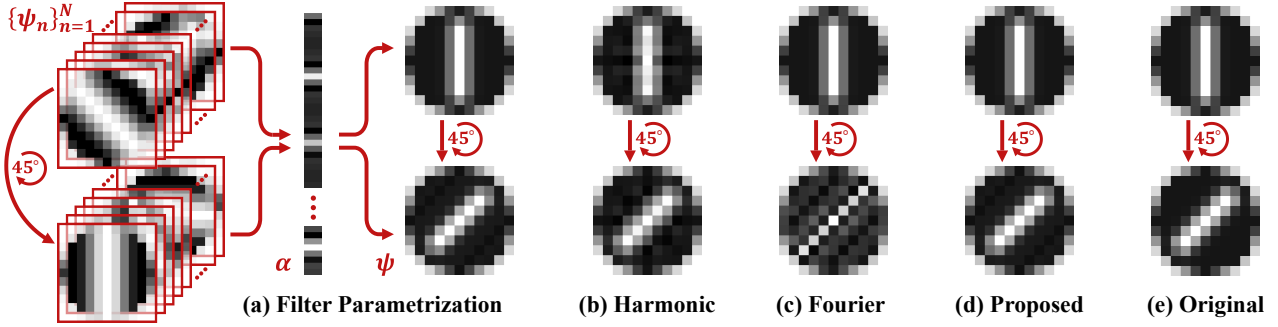


Fig. 1. (a) Illustration of filter parametrization by linear combination of basis functions, and the filter rotation based on it. All the filters are with circular shape masks for better rotation. (b)-(d) The representations (upper) and correlated $\pi/4$ rotations (lower) of a given 2D filter, by adopting harmonics bases [3], 2D Fourier bases [8] and the proposed bases as the basis functions, respectively. (e) The original filter (upper) and its $\pi/4$ rotation (lower).

clients [9]. Then, as the example shown in Fig. 1 (a), one can rotate the filter to arbitrary degrees by rotating the basis functions in continuous domain and use it to construct rotation equivariant convolutions.

Albeit achieving good development in preserving rotation equivariance, the current filter parametrization strategies still have evident drawbacks. The most critical one is in the accuracy of filter representation. For harmonics based steerable filters [3], [4], as shown in Fig 1(b), the harmonics based filter parametrization usually leads to over-smooth configurations on filter representation, due to the consideration of reducing over-fitting issue by avoiding using high frequency bases. Moreover, there are usually unexpected ring-shape artifacts owing to the ring-shape radial parts in harmonics based filter parametrization. As for PDO-eConv, it is just designed for 5×5 filters, and only contains 15 simple elementary filters [5]. Although it can well represent partial differential operators, it's not able to finely represent varying kinds and sizes of filters with high accuracy. The aforementioned inaccuracy issue in current filter parametrization methods tends to affect the performance of the corresponding equivariant convolutions. Especially, this issue will be more severe in low-level image processing tasks, where the rotation equivariance of local features is important, but still has not been fully and accurately explored yet, calling for a practicable equivariant convolution method.

Against the above issue, this study presents a new filter parametrization method for equivariant convolution designing. The contribution of this work can be mainly summarized as follows:

1) We design a new set of atomic basis functions for filter parametrization, which largely alleviates the over-smooth problem and fence effect¹ existed in current research simultaneously. Specifically, we design an enhanced version of 2D fourier series expansion in filter parametrization. When the rotation degree is $k\pi/2$ ($k \in \mathbb{N}$), as shown in Fig. 1 (c) and (d), the proposed basis functions are exactly equivalent to the commonly used 2D fourier basis functions. In this case, the proposed filter parametrization method is equivalent to 2D inverse discrete Fourier transform, which ensures that any discrete filter can be represented with

¹The fence effect here means that the interpolation of two observed grid points (achieved by filter parametrization) is incorrect, which will lead to an incorrect rotation result. Please refer to Section 3 for more details and analysis.

no error. Besides, when the rotation degree is other than $k\pi/2$ ($k \in \mathbb{N}$), the proposed filter parametrization can largely alleviate the fence effect that usually occurs in conventional 2D fourier series expansion, inclining to highly improve the representation capability of filter parametrization for both low-level and high-level tasks.

2) With the proposed filter parametrization, we construct a new equivariant convolution method, named Fourier series expansion based equivariant convolution (F-Conv). We prove that the equivariance of F-Conv is exact in the continuous domain, while becoming approximate only after the discretization. Moreover, we provide error analysis for the case when the equivariance is approximate, showing that the approximation error is dependent on the mesh and filter sizes, complying with our common sense for this task.

3) Experiments have been implemented on typical high-level and low-level image processing tasks to evaluate the performance of the proposed method. Particularly, rather than conventional filter parametrization literatures less involving low-level image processing experiments, this work applies filter parameterized equivariant convolutions to the low-level image super-resolution task for the first time, and achieves evidently better performance than conventional filter parametrization based equivariant convolutions. This reveals the possibility of filter parametrization based equivariant convolutions on the local image feature preservation, and the potential usefulness of this methodology to wider range of applications.

The paper is organized as follows. Section 2 reviews the related works and introduces some necessary prior knowledge. Section 3 presents the proposed filter parametrization framework with theoretical analysis on its properties. Based on this filter parametrization method, Section 4 presents the F-Conv method on continuous functions and discrete domain, respectively. Section 5 then demonstrates experimental results implemented on typical high-level classification and low-level image super-resolution tasks, to substantiate the superiority of the proposed method both visually and quantitatively. The paper is finally concluded with a future work discussion.

2 RELATED WORK AND PRIOR KNOWLEDGE

2.1 Equivariant CNNs

Early attempts for exploiting transformation symmetry prior in images are mainly designed by heuristics [10], [11],

[12], [13]. Data augmentation [10] is the most commonly used one among them. The idea is to enrich the training set with transformed samples to train a model that is robust to the transformations. Besides, TI-Pooling [11] applied the transformation invariant pooling operator to the outputs of parallel architectures for the considered transformation set. [12], [14] further transformed feature maps with differentiable modules to enforce equivariance transformations. This category of approaches learns the transformation invariance directly from data, which, however, demands for a relatively large number of parameters and makes the network prone to overfitting.

Recent works along this line focus on incorporating transformation equivariance directly into network's elemental architectures, i.e., equivariant convolutions. Typically, [6] exploited the fact that $\pi/2$ degree rotation and reflection on square lattice can be easily implemented by changing the position of elements in a filter, and proposed G-CNN with $\pi/2$ degree rotation and reflection equivariant (i.e. $p4$ and $p4m$) on square lattices. By replacing the commonly used square lattices with hexagonal lattices, HexaConv succeeded in expanding rotation equivariant to $\pi/3$ degree rotation ($p6m$) [7]. Nevertheless, it is hard to make CNNs equivariant to the rotation angles other than $\pi/2$ and $\pi/3$ degrees in this intuitive way as [6] and [7] did, since it is not easy to design other rotational symmetric discrete lattices on the 2D plane. In order to exploit more symmetries, [15] and [16] produced feature maps and filters at different orientations with bilinear interpolation, achieving an inherently approximately equivariant. [17] used harmonics to extract features and obtain 360° equivariance. However, in these methods, the expected equivariance cannot be theoretically guaranteed after Gaussian-resampling or bilinear interpolation.

Very recently, the filter parametrization technique has been employed for designing equivariant CNNs. [3] and [4] make early attempts by employing harmonics as steerable filters to achieve exact equivariance with respect to larger transformation groups in continuous domain. Afterwards, [5] and [18] designed equivariant by relating convolutions with partial differential operators and proposed PDO-eConv, and firstly provided the error analysis to the approximation in the discrete domain. The key drawback of these filter parametrization methods is in the accuracy of filter representation. Specifically, for harmonics based method, the maximum angular frequencies for each radial part of harmonics are hard to choose, and one usually has to select lower angular frequencies to alleviate fence effect, which will then easily lead to over-smooth issue. Besides, the ring-shape radial parts may be not well linked together, which tends to conduct unexpected ring-shape artifacts. As for PDO-eConv, it is specifically designed for 5×5 filters, with limited and relatively simple elementary filters [5]. It is thus hard to sufficiently represent varying kinds and sizes of filters with high accuracy. Such inaccurate-representation issue might less affect the performance of high-level computer vision tasks, which mainly require relatively coarse-scale transformation equivariance knowledge. However, for low-level problems, one has to consider to represent much finer-grained local details in pixel level with higher accuracy requirement, which makes current filter parametrization regimes hardly be used effectively.

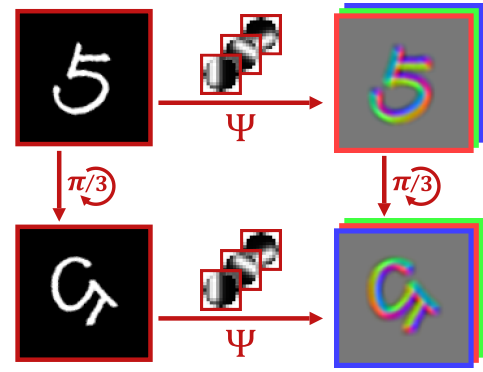


Fig. 2. Illustration of the rotation equivariance of Ψ , where the rotation group size is 3.

2.2 Prior Knowledge about Equivariance

We follow the equivariance of prior works: equivariance of a mapping transform means that a transformation on the input will result in a predictable transformation on the output [4], [5]. Specifically, let Ψ be a mapping from the input feature space to the output feature space, and G is a group of transformations. We say Ψ is group equivariance about G , if for any $g \in G$,

$$\Psi[\pi_g[f]] = \pi'_g[\Psi[f]], \quad (1)$$

where f can be any input feature map in the input feature space, π_g and π'_g denote how the transformation g acts on input and output features, respectively.

In this paper, we focus on the rotation equivariance on 2D convolutions². In this case, G is a group of rotation transformations, and Ψ is a convolution mapping. As shown in Fig. 2, the equivariance can be easily understood as: rotating an input feature map will result to the corresponding output feature map rotated with the same degree as input.

3 FILTER PARAMETRIZATION FRAMEWORK

Filter parametrization is one of the most important concepts for the realization of equivariant convolution. Therefore, we first introduce the proposed basis function set and then adopt it to construct a new filter parametrization method.

As shown in Fig. 1(a), the basic idea of filter parametrization is to define the objective functional filter as the linear combination of a set of basis functions $\{\psi_n\}_{n=1}^N$, aiming to get a learnable functional filter $\psi : \mathbb{R}^2 \rightarrow \mathbb{R}$. Formally, it can be expressed as [3], [9]:

$$\psi(x) = \sum_{n=1}^N w_n \psi_n(x), \quad (2)$$

where $x = [x_1, x_2]^T \in \mathbb{R}^2$ denotes the 2 spatial coordinates, N is the number of basis functions, w_n is the n -th coefficient. Moreover, the rotation operator π_θ can be easily expressed by coordinate transformation, that is:

$$\pi_\theta[\psi](x) = \psi(U_\theta^{-1}x), \text{ where } U_\theta = \begin{bmatrix} \cos(\theta) & \sin(\theta) \\ -\sin(\theta) & \cos(\theta) \end{bmatrix}, \quad (3)$$

where $\theta \in (-\pi, \pi]$ denotes the rotation angle and π_θ represents the θ degree rotation operator. In practice, the rotation

²The proposed method can be easily extended to rotation+reflection equivariance as previous works [3], [5], [6] did.

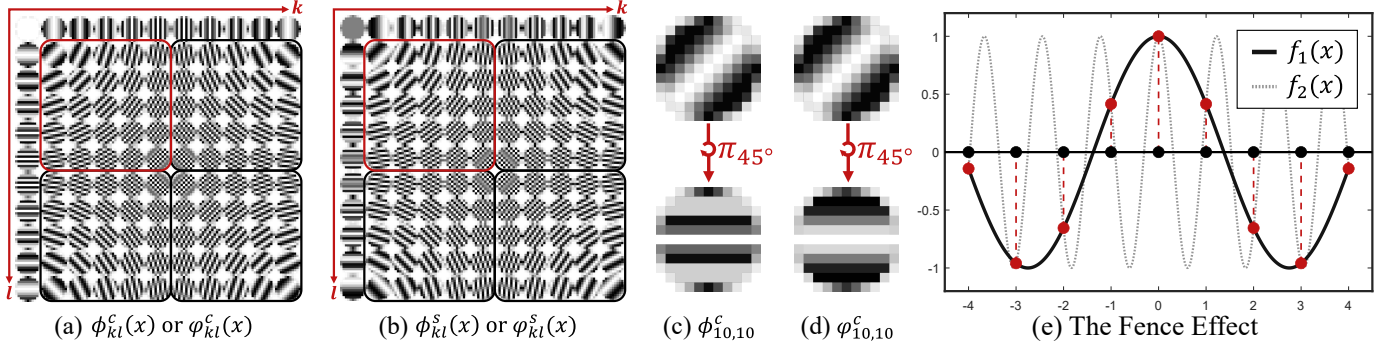


Fig. 3. (a)-(b) Illustrations of the bases ϕ_{kl}^c , φ_{kl}^c , ϕ_{kl}^s and φ_{kl}^s , with $p = 11$, $k, l = 0, 1, \dots, p - 1$. Note that for odd p , $\phi_{kl}^c = \varphi_{kl}^c$ and $\phi_{kl}^s = \varphi_{kl}^s$. The discretization of high frequency bases in black boxes are symmetrical to the low frequency bases in red box. (c)-(d) illustration of rotating $\phi_{10,10}^c$ and $\varphi_{10,10}^c$ by 45° . Note that obvious fence phenomenon can be observed in $\pi_{45}^\circ[\phi_{10,10}^c]$, while very little fence phenomenon can be seen in $\pi_{45}^\circ[\varphi_{10,10}^c]$. (e) An 1D example showing the reason resulting in the fence effect: $\forall x \in \mathbb{N}$, $f_1(x) = f_2(x)$, where $f_1(x) = \cos(2\pi/10 \cdot 2x)$, $f_2(x) = \cos(2\pi/10 \cdot 9x)$. Although the discretization of the two functions are the same, the discretization of the transformation results of the high frequency one tends to be highly unpredictable.

operator is usually adopted on the bases instead of the filter itself, that is

$$\pi_\theta[\psi](x) = \sum_{n=1}^N w_n \pi_\theta[\psi_n](x) = \sum_{n=1}^N w_n \psi_n(U_\theta^{-1}x). \quad (4)$$

Previous researches have exploited different types of basis set for filter parametrization, such as harmonics, partial-differential-operator-like and polynomial bases [3], [4], [5], [19]. In this study, we aim to construct a new basis set to enhance the representation accuracy of filter parametrization with rotation equivariance along this research line.

2D Fourier bases. 2D discrete Fourier transform (DFT) has been applied to many low-level visual tasks, and attained great success for its easy calculation and high representation accuracy. Since the DFT and inverse DFT can be written as Fourier series expansion, it is natural to construct a Fourier series expansion based filter parametrization method. In specific, we consider a $p \times p$ discrete filter $\tilde{\phi}$ as the discretization of an underlying 2D function $\phi(x)$, and it is sampled uniformly on the $[-(p-1)h/2, (p-1)h/2]^2$ area of \mathbb{R}^2 , where h represents the mesh size of images. Formally, the 2D Fourier bases (with a circular shape mask for better performing rotation) can be denoted as follows [20]:

$$\begin{aligned} \phi_{kl}^c(x) &= \Omega(x) \cos\left(\frac{2\pi}{ph}[k, l] \cdot \begin{bmatrix} x_1 \\ x_2 \end{bmatrix}\right), \\ \phi_{kl}^s(x) &= \Omega(x) \sin\left(\frac{2\pi}{ph}[k, l] \cdot \begin{bmatrix} x_1 \\ x_2 \end{bmatrix}\right), \end{aligned} \quad (5)$$

where $k, l = 0, 1, \dots, p - 1$, “ \cdot ” denotes the matrix multiplication, and $\Omega(x) \geq 0$ is a radial mask function³ that satisfies $\Omega(x) = 0$ if $\|x\| \geq (p+1/2)h$. For intuitive understanding of (5), illustrations of Fourier bases are shown in Fig. 3 (a)-(b). Then, the real part of 2D inverse DFT for $\tilde{\phi}$ (with circular shape mask) can be expressed in following Fourier series expansion form:

$$\phi(x) = \sum_{k=0}^{p-1} \sum_{l=1}^{p-1} (a_{kl} \phi_{kl}^c(x) + b_{kl} \phi_{kl}^s(x)), \quad (6)$$

³Please refer to the supplementary material for detail settings of radial mask function $\Omega(x)$.

where a_{kl} and b_{kl} are expansion coefficients. (6) is a specific case of (2), which means it is also a filter parametrization.

Eq. (6) can represent any discrete filter $\tilde{\phi}$ (masked into circular shape) with zero representation error⁴. This is because, one can set coefficients a_{kl} and b_{kl} as DFT results of $\tilde{\phi}$, and then inverse DFT can restore $\tilde{\phi}$ with zero error. Besides, it is easy to deduce that $\Omega(x)$ doesn't affect the Fourier series expansion for x s.t. $\Omega(x) \neq 0$. Thus, Eq. (6) seems to be a rational filter parametrization.

However, when we use this basis set to represent a rotated filter by Eq. (4), the rotation result is usually unsatisfying, as shown in Fig. 1(c). The incorrect rotation result is due to the fact that although Fourier series expansion can represent any discrete filter with zero error, the interpolation between two discrete points may still be incorrect. In this paper, this type of quality degradation during the rotation is called fence effect.

Moreover, as shown in Fig. 3 (c), the fence effect will cause some of the Fourier bases to be badly destroyed after rotation by (3). Since these fence effects tend to seriously hamper the accuracy for representing the rotated filer, such basis function set is not suggested to be directly employed for designing filter parametrization methods.

Proposed bases and filter parametrization. The key issue now is to alleviate the unexpected fence effect in Fourier series expansion for the rotated cases, while possibly keep its high accuracy for the rotation free cases. Firstly, let us have a look at the 1D example depicted in Fig. 3 (e) for easily understanding the fence effect. From the figure, we can see that high frequency cosine function and low frequency cosine function can result in the same discretization, and the high frequency one might possibly conduct inaccuracy when it is resampled after transformations. Such fence effect also easily occurs for the commonly used 2D Fourier series expansion since after discretization, 2D Fourier bases with high frequencies will be depicted similar to those with low frequencies, as clearly depicted by the bases in the lower right corner of Fig. 3 (a) and (b). The discretization of such bases will then be badly destructed after rotation, as shown in Fig. 3 (c).

⁴Zero representation error means $\tilde{\phi}_{kl} = \phi(x_{kl})$, where x_{kl} is the coordinate to the element of $\tilde{\phi}$ in its k row and l column.

Against this issue, we exploit the symmetry of bases in 2D Fourier base set to construct new base set. As shown in Fig. 3, the bases of the four areas (marked with boxes in red and black colors) in Fig. 3 (a) and (b) are symmetrical. This means that we can use the mirror functions of low frequency bases (in the red boxes) to replace the high frequency bases (in the black boxes) which intrinsically cause the fence effect. For example, when $p = 11$, for $l = 0, 2, \dots, p-1$, we can use $\cos\left(\frac{2\pi}{ph}(-2x_1 + lx_2)\right)$ to replace $\cos\left(\frac{2\pi}{ph}(9x_1 + lx_2)\right)$, since their discretizations are the same to each other. Specifically, the proposed bases are in following forms:

$$\begin{aligned}\varphi_{kl}^c(x) &= \Omega(x) \cos\left(\frac{2\pi}{ph}[\mathcal{I}_p(k), \mathcal{I}_p(l)] \cdot \begin{bmatrix} x_1 \\ x_2 \end{bmatrix}\right), \\ \varphi_{kl}^s(x) &= \Omega(x) \sin\left(\frac{2\pi}{ph}[\mathcal{I}_p(k), \mathcal{I}_p(l)] \cdot \begin{bmatrix} x_1 \\ x_2 \end{bmatrix}\right),\end{aligned}\quad (7)$$

where $k, l = 0, 1, \dots, p-1$, $\Omega(x)$ is the aforementioned radial mask function, and for any integer m ,

$$\mathcal{I}_p(m) = \begin{cases} m & \text{if } m \leq p/2 \\ m-p & \text{if } m > p/2 \end{cases}. \quad (8)$$

Based on the proposed bases (7), the filter parametrization for a filter $\tilde{\varphi}$ is with the following expression:

$$\varphi(x) = \sum_{k=0}^{p-1} \sum_{l=1}^{p-1} (a_{kl} \varphi_{kl}^c(x) + b_{kl} \varphi_{kl}^s(x)), \quad (9)$$

where a_{kl} and b_{kl} are expansion coefficients, which are learnable in training process when we exploit $\varphi(x)$ in convolutions.

To analyze the properties of the proposed bases, we first deduce the following theorem⁵:

Theorem 1. For any mesh size $h \in \mathbb{R}$, filter size $p \in \mathbb{N}_+$, and grid point x on the $p \times p$ mesh of $[(1-p)h/2, (p-1)h/2]^2$, i.e., $x_1 = (i - (p-1)/2)h$, $x_2 = (j - (p-1)/2)h$, $\forall i, j = 0, 1, \dots, p-1$, let $k, l = 0, 1, \dots, p-1$, then,

$$\begin{aligned}\varphi_{kl}^c(x) &= s(p, k, l) \cdot \phi_{kl}^c(x), \\ \varphi_{kl}^s(x) &= s(p, k, l) \cdot \phi_{kl}^s(x),\end{aligned}\quad (10)$$

where φ_{kl}^c and φ_{kl}^s are defined in (7), ϕ_{kl}^c, ϕ_{kl}^s are defined in (5), $s(p, k, l) \in \{-1, 1\}$, satisfying $s(p, k, l) = \text{sign}(k - p/2 + \epsilon)^{p-1} \cdot \text{sign}(l - p/2 + \epsilon)^{p-1}$, $0 < \epsilon < 1/2$.

From Theorem 1, it is easy to see that, the proposed basis set is exactly equivalent to commonly used 2D Fourier bases when there is no rotation (or other transformations). Specifically, if p is an odd number, we can obtain $s(p, k, l) = 1$, implying that the proposed basis set is exactly the same as the 2D Fourier bases, as shown in Fig. 3 (a) and (b). When p is an even number, we still have $|s(p, k, l)| = 1$, and then the proposed bases are equivalent to the 2D Fourier bases, just some of their expansion coefficients are with opposite signs. Therefore, the proposed filter parametrization is equivalent to inverse 2D DFT when there is no rotation, and there is no representation error in this case.

Moreover, it is also easy to deduce that the fence effect can be largely alleviated when we rotate the proposed bases with Eq. (3). It should be noted that the largest frequency

⁵The proofs of all the theorems in this paper are presented in supplementary material.

of the commonly used 2D Fourier bases (5) is $\frac{p-1}{ph}$, i.e., the smallest period is $\frac{p}{p-1}h \approx h$. This implies that there is not zero possibility to simultaneously exist one peak and one valley between two grid points, which intrinsically leads to the heavy fence effect in rotation results as shown in Fig. 3(c). As comparison, the largest frequency of the proposed bases is $\max_{k \in \{1, \dots, p\}} \{ \mathcal{I}_p(k)/ph \} \leq 1/2h$, i.e., the smallest period is $2h$. Therefore, there is at most one peak or valley between two grid points in any of the proposed bases⁶, which will help alleviating the fence effect when rotating the bases, as shown in Fig. 3(d).

According to the above analysis, the proposed filter parametrization not only is able to faithfully keep the high accuracy of 2D Fourier bases, but also well weakens the issue of the fence effect. In the following, we will introduce the equivariant convolutions based on these bases.

4 EQUIVARIANT CONVOLUTION FRAMEWORK

In this section, we first introduce some necessary concepts and the sketchy framework of the proposed equivariant convolutions. Then, we introduce the proposed equivariant convolutions in the continuous domain, and theoretically prove that the rotation equivariance is exact. Finally, we adopt the proposed equivariant convolutions to the discrete domain and provide error analysis for it.

4.1 Related Concepts and Sketchy Framework

Firstly, let's introduce some necessary concepts and notations. The proposed equivariant convolutions, F-Conv, follow the overall framework of previous works [3], [4], [5]. Specifically, we represent an image as a two-dimensional grid function $I \in \mathbb{R}^{n \times n}$, and represent an intermediate feature map as F . Note that in rotation equivariant networks, a feature map is a multi-channel matrix (i.e., a tensor), as shown in Fig. 4 (a), with $F \in \mathbb{R}^{n \times n \times t}$, where the third mode is with respect to the rotation group S , and t is the number of elements in S . Moreover, we denote a specific channel in F as $F^A \in \mathbb{R}^{n \times n}$, where $A \in S$ is a rotation matrix, and also used as an index for denoting a specific channel in F .

Besides, the filters in rotation equivariant networks also contain modes with respect to S (indexed by A or $B \in S$) as shown in Fig. 4. In specific, it is easy to see that the t slices in a tensor of filters, are similar to each other along the third mode, except rotated to different angles. In the proposed method, the key idea to achieve filters in this pattern is to adopt the proposed filter parametrization on them, with Eq. (9). More specifically, we achieve a set of filters rotated along the third mode by discretizing the rotations of a single functional filter, i.e., for any $A \in S$, we set the slice of the filter indexed by A in the third mode as the discretization of $\varphi(A^{-1}x)$. In this way, we can train t filters in different angles by only learning a set of expansion coefficients of $\varphi(x)$, and construct the equivariant convolutions.

In the following section, we will first introduce the F-Conv on continuous functions, which can be regarded as the ideal case (mesh size $h \rightarrow 0$) of the commonly used

⁶Half period of cosine and sine functions can only contain one peak or valley.

TABLE 1

The involved concepts and notations for equivariant convolutions (eConv) in the continuous and discrete domains, respectively.

Concept	Notation	
	Continuous	Discrete
Input Image	$r(x)$	I
Transformation Group	$O(2)$	S
Group element/Index	$A, B \in O(2)$	$A, B \in S$
Feature Map	$e(x, A)$	F^A
Filter (Input)	$\varphi_{in}(A^{-1}x)$	$\tilde{\Psi}^A$
Filter (Intermediate)	$\varphi_A(B^{-1}x)$	$\tilde{\Phi}^{B,A}$
Filter (Output)	$\varphi_{out}(B^{-1}x)$	$\tilde{\Upsilon}^B$
eConv (Input)	$\Psi[r]$	$\tilde{\Psi} \star I$
eConv (Intermediate)	$\Phi[e]$	$\tilde{\Phi} \star F$
eConv (Output)	$\Upsilon[e]$	$\tilde{\Upsilon} \star F$

convolution on digital images. Correspondingly, the continuous version of I and F^A are denoted as 2-dimensional functions $r(x)$ and $e(x, A)$, $x \in \mathbb{R}^2$. Although continuous F-Conv can not be directly utilized in practice, theoretical analysis in continuous domain should facilitate to more easily understanding the insights underlying the F-Conv, while alleviates the complexity and approximation error caused by the discretization.

In Section 4.3, we will formally introduce the discretized F-Conv, which is the practically available version. To avoid the possible confusion cased by different notations in continuous and discrete domains, we list the major notations correspondingly used in two domains in Table 1.

4.2 Equivariant Convolution on Continuous Functions

For convolutional networks, the input image and intermediate feature map can be naturally modeled as functions defined in the continuous domain⁷.

Following the previous works [4], [5], we denote the orthogonal group as $O(2)$, and consider the equivariance on it⁸. Formally, $O(2) = \{A \in \mathbb{R}^{2 \times 2} | A^T A = I_{2 \times 2}\}$, which contains all rotation and reflection matrices. Without ambiguity, we use A to parameterize $O(2)$. We consider the Euclidean group $E(2) = \mathbb{R}^2 \rtimes O(2)$ (\rtimes is a semidirect-product), whose element is represented as (x, A) . Restricting the domain of A and x , we can also use this representation to parametrize any subgroup of $E(2)$, such as the rotation group.

We then model the network input image as a function defined on \mathbb{R}^2 , denoted as $r(x)$, and model the intermediate feature map as a function defined on $E(2)$, denoted as $e(x, A)$ (as shown in Table 1, $r(x)$ and $e(x, A)$ are the continuous versions of I and F^A in Fig. 4, respectively). A feature map e can also be viewed as a set of functions defined on \mathbb{R}^2 with infinite channels indexed by A . We denote the function spaces of r and e as $C^\infty(\mathbb{R}^2)$ and $C^\infty(E(2))$, respectively⁹. Then, transformations on inputs and feature maps can be

⁷In this paper, we only consider the 2D case, which can be easily generalized to n dimensional cases.

⁸ S is a subgroup of $O(2)$, and it is also regarded as the discretization of $O(2)$ in this paper.

⁹The smoothness of e means that the feature map $e(x, A)$ is smooth with respect to x when A is fixed. For simplicity, we set the functional space as $C^\infty(\mathbb{R}^2)$. Actually, in implementation, we only require that $r \in C^2(\mathbb{R}^2)$. The requirement on e is the same.

mathematically formulated. For an input $r \in C^\infty(\mathbb{R}^2)$ and transformation $\tilde{A} \in O(2)$, \tilde{A} acts on r by

$$\pi_{\tilde{A}}^R[r](x) = r(\tilde{A}^{-1}x), \forall x \in \mathbb{R}^2. \quad (11)$$

For a feature map $e \in C^\infty(E(2))$ and transformation $\tilde{A} \in O(2)$, \tilde{A} acts on e by

$$\pi_{\tilde{A}}^E[e](x, A) = e(\tilde{A}^{-1}x, \tilde{A}^{-1}A), \forall (x, A) \in E(2). \quad (12)$$

In this way, we can construct parameterized convolutions as Eq. (9) for input layer, intermediate layers (group-convolutional layers) and output layer, respectively. Note that the discrete version of these convolutions are shown in Fig. 4 for easy understanding.

Input layer. We use Ψ to denote the convolution imposed on the input layer, which maps an input $r \in C^\infty(\mathbb{R}^2)$ to a feature map defined on $E(2)$. Specifically, for any $(y, A) \in E(2)$, we define:

$$\Psi[r](y, A) = \int_{\mathbb{R}^2} \varphi_{in}(A^{-1}x) r(y - x) d\sigma(x), \quad (13)$$

where σ is a measure on \mathbb{R}^2 and φ_{in} is a parameterized filter defined in the formulation of (9). Note that (13) can be roughly viewed as convoluting $r(x)$ with a set of transformed filters, $\{\varphi_{in}(A^{-1}x) | A \in O(2)\}$.

Intermediate layers. We use Φ to denote the convolution on an intermediate layer, which maps a feature map $e \in C^\infty(E(2))$ to another feature map defined on $E(2)$. Specifically, for any $(y, B) \in E(2)$, we define:

$$\Phi[e](y, B) = \int_{\mathbb{R}^2} \int_{O(2)} \varphi_A(B^{-1}x) e(y - x, BA) d\sigma(x) dv(A), \quad (14)$$

where v is a measure on $O(2)$, $A, B \in O(2)$ denote orthogonal transformations in the considered group, and φ_A indicates the filter with respect to the channel of feature map indexed by A , which is parameterized by (9).

Output layer. We use Υ to denote the convolution on the final layer, which maps a feature map $e \in C^\infty(E(2))$ to a function in $C^\infty(\mathbb{R}^2)$. Specifically, for any $y \in \mathbb{R}^2$, we define:

$$\Upsilon[e](y) = \int_{\mathbb{R}^2} \int_{O(2)} \varphi_{out}(B^{-1}x) e(y - x, B) d\sigma(x) dv(B), \quad (15)$$

where $B \in O(2)$ and φ_{out} is a parameterized filter.

We now show that the above operators are equivariant under orthogonal transformations ($O(2)$) and describe how the outputs are transformed with the transformations of inputs. Specifically, inspired by the theoretical result presented in [5], we can deduce the following theorem.

Theorem 2. For $r \in C^\infty(\mathbb{R}^2)$, $e \in C^\infty(E(2))$ and $\tilde{A} \in O(2)$, the following rules are satisfied:

$$\begin{aligned} \Psi \left[\pi_{\tilde{A}}^R[r] \right] &= \pi_{\tilde{A}}^E[\Psi[r]], \\ \Phi \left[\pi_{\tilde{A}}^E[e] \right] &= \pi_{\tilde{A}}^E[\Phi[e]], \\ \Upsilon \left[\pi_{\tilde{A}}^E[e] \right] &= \pi_{\tilde{A}}^R[\Upsilon[e]], \end{aligned} \quad (16)$$

where $\pi_{\tilde{A}}^R$, $\pi_{\tilde{A}}^E$, Ψ , Φ and Υ are defined by (11), (12), (13), (14) and (15), respectively.

Furthermore, since the convolution operators are naturally translation equivariant, it is easy to verify that the

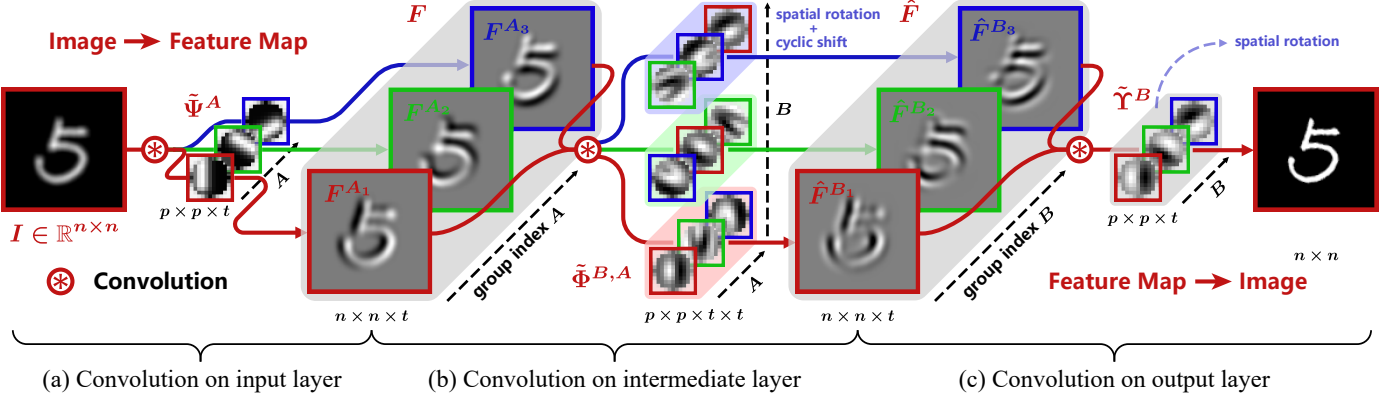


Fig. 4. Illustration of a example of network constructed by the proposed equivariant convolutions, where we set the transformation group S ($A_i, B_i \in S$) as $2\pi i/3$ rotations, $i = 1, 2, 3$. (a)-(c) Equivariant convolutions of the input layer, intermediate layers, and output layer, respectively.

proposed convolutions are equivariant over $E(2)$. Combining with nonlinearities such as ReLU, which do not disturb the equivariance, we can construct a network that preserves equivariance over the entire network.

4.3 Equivariant Convolution on Discrete Domain

Next, we show how to apply the F-Conv to 2D digital images. Formally, we assume that an image $I \in \mathbb{R}^{n \times n}$ represents a two-dimensional grid function obtained by discretizing a smooth function $r : \mathbb{R}^2 \rightarrow \mathbb{R}$ at the cell-center of a regular grid with $n \times n$ cells, i.e., for $i, j = 1, 2, \dots, n$,

$$I_{ij} = r(x_{ij}), \quad (17)$$

where $x_{ij} = ((i - \frac{n+1}{2})h, (j - \frac{n+1}{2})h)^T$, and h is the mesh size.

Similarly, an intermediate feature map $F \in \mathbb{R}^{n \times n \times t}$ in equivariant networks is a multi-channel matrix (i.e., a tensor), which can be viewed as the discretization of a continuous function defined on $\tilde{E} = \mathbb{R}^2 \times S$, where S is a subgroup¹⁰ of $O(2)$ and t is the number of elements in S . Formally, we represent F as a three-dimensional grid function sampled from a smooth function $e : \mathbb{R}^2 \times S \rightarrow \mathbb{R}$, i.e., for $i, j = 1, 2, \dots, n$,

$$F_{ij}^A = e(x_{ij}, A), \quad (18)$$

where $x_{ij} = ((i - \frac{n+1}{2})h, (j - \frac{n+1}{2})h)^T$ and $A \in S$.

Just like I , a single channel $p \times p$ filter represents a two-dimensional grid function obtained by discretizing a smooth function $\varphi : \mathbb{R}^2 \rightarrow \mathbb{R}$, which satisfies $\varphi(x) = 0, \forall x, s.t., \|x\| \geq (p+1/2)h$. Accordingly, we define filters for input, intermediate and output layers as $\tilde{\Psi} \in \mathbb{R}^{p \times p \times t}$, $\tilde{\Phi} \in \mathbb{R}^{p \times p \times t \times t}$ and $\tilde{Y} \in \mathbb{R}^{p \times p \times t}$, respectively, where t is the number of elements in S . Formally, for $i, j = 1, 2, \dots, p$, and $A, B \in S$,

$$\begin{aligned} \tilde{\Psi}_{ij}^A &= \varphi_{in}(A^{-1}x_{ij}), \\ \tilde{\Phi}_{ij}^{B,A} &= \varphi_A(B^{-1}x_{ij}), \\ \tilde{Y}_{ij}^B &= \varphi_{out}(B^{-1}x_{ij}), \end{aligned} \quad (19)$$

¹⁰In practice, the subgroup is usually assumed to contain m rotations with $2\pi/m$ degree for an integer $m \in \mathbb{N}_+$.

where $x_{ij} = ((i - \frac{p+1}{2})h, (j - \frac{p+1}{2})h)^T$, φ_{in} , φ_{out} and $\varphi_A, \forall A \in S$ are parameterized filters defined in the formulation of (9), and φ_A indicates the filter with respect to the channel of feature map indexed by A . One can see Fig. 4 for easy understanding of these filters.

It should be noted that the filters in (19) can be learnt by calculating the expansion coefficients as shown in (9). For example, for any $A \in S$, $\tilde{\Psi}^A$ shares a set of representation coefficients, and can be obtained by learning the coefficients of the bases $\{\varphi_{kl}^{cA}, \varphi_{kl}^{sA} | k, l = 0, 1, \dots, p-1\}$, where

$$\begin{aligned} \left(\tilde{\varphi}_{kl}^{cA}\right)_{ij} &= \varphi_{kl}^c(A^{-1}x_{ij}) \\ \left(\tilde{\varphi}_{kl}^{sA}\right)_{ij} &= \varphi_{kl}^s(A^{-1}x_{ij}). \end{aligned} \quad (20)$$

Accordingly, we can then discretize the proposed continuous convolution operators for input layer, intermediate layers and output layer (i.e., (13), (14) and (15)), as follows¹¹, where we define $x_{ij} = ((i - \frac{p+1}{2})h, (j - \frac{p+1}{2})h)^T$ and $y_{ij} = ((i - \frac{n+p+2}{2})h, (j - \frac{n+p+2}{2})h)^T$.

Input layer. We use the discretization of Eq. (13) to deal with the input layer, and construct the equivariant convolution for the input layer. For any $A \in S$ and $i, j = 1, 2, \dots, n$, the convolution of $\tilde{\Psi}$ and I is

$$\begin{aligned} \left(\tilde{\Psi} \star I\right)_{ij}^A &= \sum_{(\tilde{i}, \tilde{j}) \in \Lambda} \varphi_{in}\left(A^{-1}x_{\tilde{i}\tilde{j}}\right) r\left(y_{ij} - x_{\tilde{i}\tilde{j}}\right) \\ &= \sum_{(\tilde{i}, \tilde{j}) \in \Lambda} \tilde{\Psi}_{ij}^A I_{i-\tilde{i}, j-\tilde{j}}, \end{aligned} \quad (21)$$

where Λ is a set of indexes, denoted as $\Lambda = \{(i, j) | i, j = 1, 2, \dots, p\}$. It is easy to deduce that (21) can also be more concisely written as

$$\left(\tilde{\Psi} \star I\right)^A = \tilde{\Psi}^A * I, \quad (22)$$

where $*$ is the common 2D convolution. One can see Fig 4 (a) for easy understanding this convolution.

Intermediate layers. For intermedate layers, we use the discretization of (14) to construct the discrete equivariant

¹¹All the convolutions considered following are with appropriate padding at the edge of images.

convolutions. For any $B \in S$ and $i, j = 1, 2, \dots, n$, the convolution of $\tilde{\Phi}$ and F is

$$\begin{aligned} (\tilde{\Phi} \star F)_{ij}^B &= \sum_{(\tilde{i}, \tilde{j}) \in \Lambda, A \in S} \varphi_A(B^{-1}x_{\tilde{i}\tilde{j}}) e(y_{ij} - x_{\tilde{i}\tilde{j}}, BA) \\ &= \sum_{(\tilde{i}, \tilde{j}) \in \Lambda, A \in S} \tilde{\Phi}_{ij}^{B,A} F_{i-\tilde{i}, j-\tilde{j}}^{BA}, \end{aligned} \quad (23)$$

where $\Lambda = \{(i, j) | i, j = 1, 2, \dots, p\}$. More concisely, (23) can be equivalently reformulated as

$$(\tilde{\Phi} \star F)_{ij}^B = \sum_{A \in S} \tilde{\Phi}^{B,A} * F^{BA}. \quad (24)$$

The implementation of (24) is relatively more complex, since there is a channel shift of F caused by adopting B on its channel indexes. Therefore, we will further introduce the implementation detail of this convolution in the later sections. So far, one can see Fig 4 (b) for a sketchy understanding of this equivariant convolution.

Output layer. At the final layer we extract the information of interest for the specific task. For the rotation-invariant classification or segmentation task, the output layer can be easily set as a pooling over the orientation dimension [3], [4], [5]. While for a low-level image processing task, the convolution is necessary for the output layer. We use the discretization of (14) to construct the discrete equivariant convolution for the output layer. For $i, j = 1, 2, \dots, n$, the convolution of $\tilde{\Upsilon}$ and F is

$$\begin{aligned} (\tilde{\Upsilon} \star F)_{ij} &= \sum_{(\tilde{i}, \tilde{j}) \in \Lambda, B \in S} \varphi_{out}(B^{-1}x_{\tilde{i}\tilde{j}}) e(y_{ij} - x_{\tilde{i}\tilde{j}}, B) \\ &= \sum_{(\tilde{i}, \tilde{j}) \in \Lambda, B \in S} \tilde{\Upsilon}_{ij}^B F_{i-\tilde{i}, j-\tilde{j}}^B, \end{aligned} \quad (25)$$

where $\Lambda = \{(i, j) | i, j = 1, 2, \dots, p\}$. It can deduce that (25) can also be concisely rewritten as

$$\tilde{\Upsilon} \star F = \sum_{B \in S} \tilde{\Upsilon}^B * F^B. \quad (26)$$

One can see Fig 4 (c) for easy understanding this equivariant convolution.

We call the convolutions denoted by (21), (23) and (25) as Fourier series expansion based equivariant convolution or F-Conv, since the filters are parameterized based on Fourier series expansion.

Although we have proved that the equivariance of continuous convolutions (13), (14) and (15) are exact, their discretization still contain approximation errors. We then make an error analysis for the proposed F-Conv.

Firstly, we denote the transformations on I and F by

$$\begin{aligned} (\tilde{\pi}_{\tilde{A}}^R(I))_{ij} &= \pi_{\tilde{A}}^R[r](x_{ij}), \\ (\tilde{\pi}_{\tilde{A}}^E(F))_{ij}^A &= \pi_{\tilde{A}}^E[e](x_{ij}, A), \\ \forall i, j &= 1, 2, \dots, n, \forall A, \tilde{A} \in S. \end{aligned} \quad (27)$$

Then, we deduce the following theorem for evaluating approximation errors of the equivariance.

Theorem 3. Assuming an image $I \in \mathbb{R}^{n \times n}$ is discretized from the smooth function $r : \mathbb{R}^2 \rightarrow \mathbb{R}$ by (17), a feature map $F \in$

$\mathbb{R}^{n \times n \times t}$ is discretized form the smooth function $e : \mathbb{R}^2 \times S \rightarrow \mathbb{R}$ by (18), $|S| = t$, filters $\tilde{\Psi}$, $\tilde{\Phi}$ and $\tilde{\Upsilon}$ are generated from φ_{in} , φ_{out} and φ_A , $\forall A \in S$, by (19), respectively. If for any $A \in S$, $x \in \mathbb{R}^2$, the following conditions are then satisfied:

$$\begin{aligned} |r(x)|, |e(x, A)| &\leq F_1, \\ \|\nabla r(x)\|, \|\nabla e(x, A)\| &\leq G_1, \\ \|\nabla^2 r(x)\|, \|\nabla^2 e(x, A)\| &\leq H_1, \\ |\varphi_{in}(x)|, |\varphi_A(x)|, |\varphi_{out}(x)| &\leq F_2, \\ \|\nabla \varphi_{in}(x)\|, \|\nabla \varphi_A(x)\|, \|\nabla \varphi_{out}(x)\| &\leq G_2, \\ \|\nabla^2 \varphi_{in}(x)\|, \|\nabla^2 \varphi_A(x)\|, \|\nabla^2 \varphi_{out}(x)\| &\leq H_2, \\ \forall \|x\| \geq (p+1)h/2, \varphi_{in}(x), \varphi_A(x), \varphi_{out}(x) &= 0, \end{aligned} \quad (28)$$

where p is the filter size, h is the mesh size, ∇ and ∇^2 denote the operators of gradient and Hessian matrix, respectively. Then, for any $\tilde{A} \in S$, the following rules are satisfied:

$$\begin{aligned} \|\tilde{\Psi} \star \tilde{\pi}_{\tilde{A}}^R(I) - \tilde{\pi}_{\tilde{A}}^{\tilde{E}}(\tilde{\Psi} \star I)\|_{\infty} &\leq \frac{C}{2}(p+1)^2h^2, \\ \|\tilde{\Phi} \star \tilde{\pi}_{\tilde{A}}^{\tilde{E}}(F) - \pi_{\tilde{A}}^{\tilde{E}}(\tilde{\Phi} \star F)\|_{\infty} &\leq \frac{C}{2}(p+1)^2h^2t, \\ \|\tilde{\Upsilon} \star \tilde{\pi}_{\tilde{A}}^{\tilde{E}}(F) - \tilde{\pi}_{\tilde{A}}^R(\tilde{\Upsilon} \star F)\|_{\infty} &\leq \frac{C}{2}(p+1)^2h^2t, \end{aligned} \quad (29)$$

where $C = F_1H_2 + F_2H_1 + 2G_1G_2$, $\tilde{\pi}_{\tilde{A}}^R$, $\tilde{\pi}_{\tilde{A}}^{\tilde{E}}$, $\tilde{\Psi}$, $\tilde{\Phi}$ and $\tilde{\Upsilon}$ are defined by (19) and (27), the operator \star are defined in (21), (23) and (25), respectively, and $\|\cdot\|_{\infty}$ represents the infinity norm.

In practice, the conditions in Theorem 3 are easy to be satisfied, which only need the first and second derivatives of the underlying input function to be bounded. From the theorem, it is easy to see that the accuracy of equivariance is mainly dependent on the patch size, the mesh size and the group size. This fully complies with our common sense that the smaller mesh size and the fewer pixel number in a filter are, the smaller approximation error should be. When the mesh size approaches zero, the approximation error also approaches zero. Moreover, the theorem also implies that applying a rotation to the input image results in a joint spatial rotation operation and cyclic shift over the orientation indices of the feature maps.

4.4 Implementation Details

Implementation of group convolutions. Following the previous equivariant convolution methods [3], [4], [5], we parameterize the filters in a steerable function space with shared weights over filter orientations (exact filter rotations are achieved by rotating the basis functional filters in (9)). All layers are designed to be jointly translation and rotation equivariant.

The proposed convolutions for the input layer and the output one are easy to be implemented in practice, since (22) and (26) are both with the expressions of commonly used convolution¹². However, the convolution for the intermediate layers (24) is relatively complex, which is a group equivariant convolution [6]. For fast implementation, we first rewrite (24) as

$$(\tilde{\Phi} \star F)_{ij}^B = \sum_{A \in S} \tilde{\Phi}_{ij}^{B, B^{-1}A} * F^A. \quad (30)$$

¹²The convolution operations in popular softwares like TensorFlow and pytorch.

Then, it is easy to see that one can follow the previous works [3], [4], [5] to implement (30), i.e., by adopting the commonly used convolution on F and a $p \times p \times t \times t$ filter rotated spatially and shifted cyclically along the third mode, as shown in Fig. 4 (b). More specifically speaking, we prepare a filter $\tilde{\Phi} \in \mathbb{R}^{p \times p \times t \times t}$, which satisfies $\tilde{\Phi}^{B,A} = \tilde{\Phi}^{B,B^{-1}A}$. Then, Eq. (30) can be performed by convoluting $\tilde{\Phi}$ and F .

Normalization of bases in F-Conv. Formally, a set of rotated filters can be represented as $\tilde{\Psi} \in \mathbb{R}^{p \times p \times t}$, where t is the number of orientations. Let φ_n be the n -th element of $\{\varphi_{kl}^c, \varphi_{kl}^s | k, l = 1, 2, \dots, p\}$ and w_n be the n -th element of $\{a_{kl}, b_{kl} | k, l = 1, 2, \dots, p\}$, and then the parametrization of $\tilde{\Psi}$ can be represented as $\tilde{\Psi}_{ij}^A = \sum_n w_n \varphi_n^A = \sum_n w_n \varphi_n(A^{-1}, x_{ij})$. Then, we can obtain

$$\text{vec}(\tilde{\Psi}) = \begin{bmatrix} \text{vec}(\varphi_1^{A_1}) \dots \text{vec}(\varphi_n^{A_1}) \\ \vdots \quad \ddots \quad \vdots \\ \text{vec}(\varphi_1^{A_t}) \dots \text{vec}(\varphi_n^{A_t}) \end{bmatrix} \cdot \begin{bmatrix} w_1 \\ \vdots \\ w_n \end{bmatrix} \triangleq Dw, \quad (31)$$

where $\text{vec}(\cdot)$ is the vectorization operator, $D \in \mathbb{R}^{tp^2 \times 2p^2}$. In practice, we perform singular value decomposition on D , i.e., $D = U \Sigma V^T$, and replace D with $U \in \mathbb{R}^{tp^2 \times r}$, where r is the rank of D , and represent the parameterized filter by

$$\text{vec}(\tilde{\Psi}) = U \hat{w}, \quad (32)$$

where $\hat{w} = \Sigma V^T w$ is the new coefficients. This can reduce the redundant parameters and make the parameter learning more easily. It can also avoid the non-uniqueness of to-be-estimated coefficients, which is caused by the redundancy of columns in D . Besides, by (32), $\|\tilde{\Psi}\| = \|\hat{w}\|$, and this will lead to an easy initialization scheme on \hat{w} .

Initialization scheme. The weights \hat{w} are served as expansion coefficients of a fixed filter basis set rather than pixel values. An important practical issue of training deep networks is an appropriate initialization of weights \hat{w} . For convolutional networks, Glorot and Bengio [21] and He et. al. [22] came up with initialization schemes which are accepted as a standard for random weight initialization. Following [3] and [5], we adapt He's weight initialization scheme to initialize \hat{w} . And since $\|\tilde{\Psi}\| = \|\hat{w}\|$, this implies a normalization to the parametrization filter energies.

5 EXPERIMENTAL RESULTS

In this section, we first conduct simulated experiments to evaluate the representation capability of the proposed filter parametrization regime. Experimental results on classification and super-resolution tasks are then demonstrated to verify the effectiveness of the F-Conv method.

5.1 Filter Parametrization Verification

In Fig. 1 we show the superiority of the proposed bases when representing a simple filter function with rotation. Moreover, in Fig. 3, we have further depicted the advantage of the proposed bases as compared with the corresponding traditional 2D Fourier bases after imposing a rotation on them. In this section, we will show more verifications to evaluate the proposed filter parametrization method, with comparison to previous filter parametrization strategies, which are based on traditional 2D Fourier bases (Fourier),

the harmonics (harmonic) [3], [4] and partial differential operator (PDO) [5], on more complex filters under more filter sizes. The later two are actually the filter parametrization strategies exploited in state of the art equivariant convolutions, i.e., E2CNN [4] and PDO-eConv [5], respectively.

We estimate the representation coefficients by solving a least squares problem for all competing methods¹³. For example, for the general parametrization formulation (2), we estimate w_n by solving

$$\min_{w_n} \sum_{i=1}^p \sum_{j=1}^p \left(\hat{\psi}_{i,j} - \sum_{n=1}^N w_n \psi_n(x_{ij}) \right)^2 + \lambda \sum_{n=1}^N w_n^2 \quad (33)$$

where $\hat{\psi}$ is the observed discrete filter for parametrization, $x_{ij} = \left(\left(i - \frac{p+1}{2} \right) h, \left(j - \frac{p+1}{2} \right) h \right)^T$ and we set $\lambda = 10^{-10}$. It is easy to obtain the closed-form solution for this optimization problem [23].

Parametrization of continuous function. We first verify the representation capability of all compared methods on a continuous function. The exploited function is a 2D variant of Morlet wavelet [24], i.e.,

$$\psi_0(x) = \exp \left(-\frac{1}{2} \|a \odot x - b\|^2 \right) \cos(5(x_1 + b)), \quad (34)$$

where \odot denotes the elemental wise multiplication, a and b are zooming and translation parameters, respectively. Let $\hat{\psi}_{ij} = \psi_0(x_{ij})$, and then we solve w_n for all competing methods by Eq. (33).

Fig. 5 shows the representation results of (34) and the 45° rotation results achieved by the representations of all competing methods, where $a = [2, 1.5]^T$ and $b = [0.1, 0.1]^T$. For the case of $p = 11$, the PDO based method is not compared since it is only designed for 5×5 filters. It is easy to observe that in this experiment, the results of the proposed method evidently outperforms other comparison methods, with almost no difference from the ground truth. In comparison, there is obvious quality degradation in the parametrization result and its rotation for Harmonic based method. The commonly used Fourier bases can achieve an accurate parametrization result in rotation free case (similar as the proposed method). Nevertheless, its rotation result is with poor visual quality. For the comparison to PDO based filter parametrization, we also show the result of $p = 5$ case in Fig. 5 (e)-(i). It is seen that the result obtained by the proposed method perfectly preserve the shapes of the original function. Comparatively, the results by other competing methods contain more evident quality degradations.

Moreover, let $a = [2, 1.5]^T$, $b \sim N(0, 0, 1)$ and θ be randomly sampled from $[0, 2\pi]$, and we perform filter parametrization on filter $\psi_\theta = \pi_\theta[\psi_0]$, where π_θ is defined in Eq. (3). We repeat experiments for 1000 times and calculate the relative-mean-square error (RMSE) of filter parametrization and the 45° rotation achieved by parameterizations of each completing method. The results are shown in the first 4 columns of Table 2. It is easy to see that in the rotation free case, the 2D Fourier bases and the proposed bases can represent the filter with RMSE lower than 10^{-15} , where the approximation error is possibly due to the numerical error

¹³For the 2D Fourier bases and the proposed bases, we can also exploit the 2D DFT to estimate the representation coefficients.

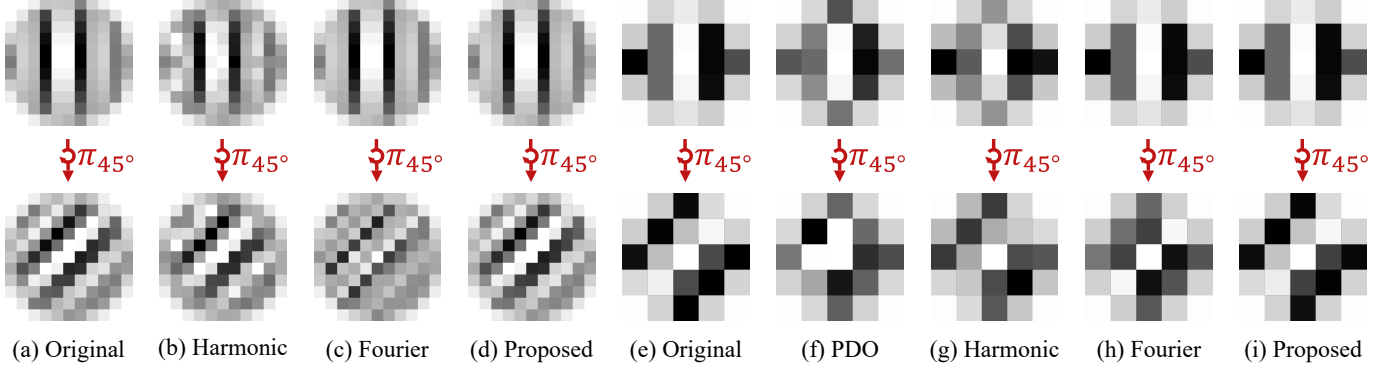


Fig. 5. (a) A discretization of the functional filter (34) and its $\pi/4$ rotation, with filter size $p = 11$ and mesh size $h = 1/5$. (b)-(d) The representations and the corresponding $\pi/4$ rotations of the given 2D filter, where harmonics bases [3], 2D Fourier bases [8] and the proposed bases are adopted as basis functions, respectively. (e) A discretization of the functional filter (34), with filter size $p = 5$ and mesh size $h = 1/2$. (f)-(i) The representations and the corresponding $\pi/4$ rotations of the given 2D filter, by adopting PDO bases [5], harmonics bases [3], 2D Fourier bases [8] and the proposed bases as basis functions, respectively.

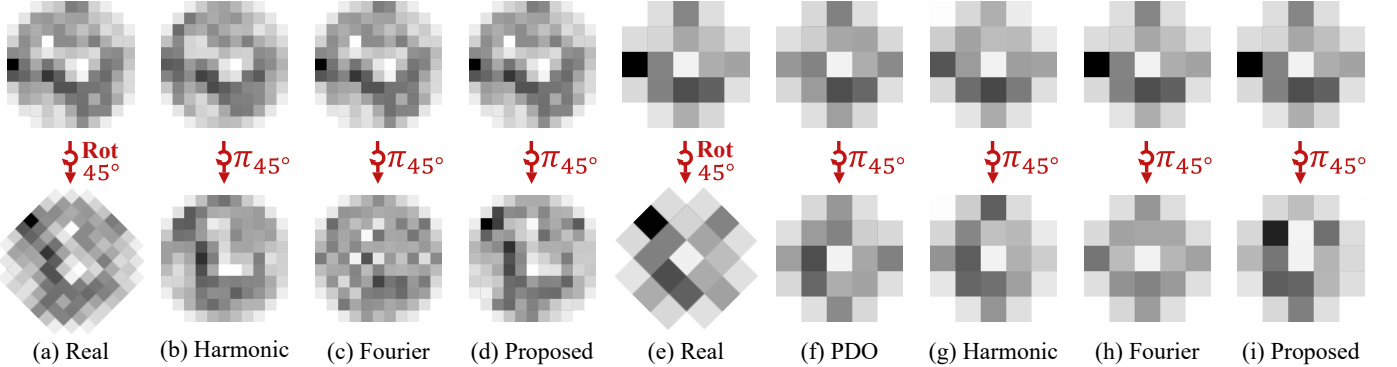


Fig. 6. (a) A discrete random filter generated by (35) and its $\pi/4$ rotation in visual, with filter size $p = 11$. (b)-(d) The representations and correlated $\pi/4$ rotations of a given 2D filter, where the harmonics bases [3], 2D Fourier bases [8] and the proposed bases are adopted as basis functions, respectively. (e) A discrete random filter generated by (35) and its $\pi/4$ rotation in visual, with filter size $p = 5$. (f)-(i) The representations and correlated $\pi/4$ rotations of a given 2D filter, by adopting PDO bases [5], harmonics bases [3], 2D Fourier bases [8] and the proposed bases as basis functions, respectively.

TABLE 2

The RMSE (mean \pm standard deviation over 1000 random generated samples) of filter parametrization results obtained by all competing methods under different filter sizes.

Method	On continuous functions				On random initializations	
	11 × 11		5 × 5		11 × 11	5 × 5
	original	45° rotation	original	45° rotation	original	original
PDO	-	-	4.5e-01 \pm 5.3e-02	1.0e-01 \pm 1.0e-01	-	5.0e-01 \pm 1.3e-01
Harmonic	3.5e-01 \pm 4.3e-02	3.6e-01 \pm 4.5e-02	4.2e-01 \pm 4.6e-02	5.5e-02 \pm 5.5e-02	4.2e-01 \pm 6.0e-02	5.3e-01 \pm 9.4e-02
Fourier	8.2e-16 \pm 1.1e-16	9.1e-01 \pm 2.4e-01	1.8e-16\pm3.9e-17	2.1e-01 \pm 2.1e-01	8.7e-16 \pm 7.5e-17	1.9e-16\pm4.4e-17
Proposed	6.0e-16\pm7.9e-17	3.9e-02\pm1.1e-02	1.9e-16 \pm 4.4e-17	2.4e-02\pm2.4e-02	7.1e-16\pm7.1e-17	2.1e-16 \pm 4.6e-17

in PC computing. When there is 45° rotation, while the Fourier bases parametrization performs relatively worse, the proposed method still evidently outperforms other competing methods.

It is should be noted that the quality degradation of local filters may not largely affect the performance in high-level tasks, like classification and segmentation, which mainly require relatively coarse-scale transformation equivariance knowledge. However, for low-level problems, one has to consider to represent much finer-grained local image details in the pixel level with higher accuracy requirement. Therefore, the proposed F-Conv is expected to show more superiority, as compared with current filter parametrization based equivariant convolutions, in low-level tasks.

Parametrization of random initialization. In practice,

filters are usually randomly initialized by independent and identically distributed distributions such as Gaussian and uniform distributions. Therefore the representation capability on random initialization is important for filter parametrization methods. Specifically, in rotation equivariant convolutions, a filter parametrization method is expected to be able to well represent and rotate the random initializations. Here, we verify all competing methods on the following randomly generated filter,

$$\hat{\psi} = \text{Resize}(\text{Gaussian}(8, 8), p), \quad (35)$$

where $\text{Gaussian}(n, n)$ is a $n \times n$ 2D patch sampled form Gaussian distribution whose mean and variance are 0 and 1, respectively, and $\text{Resize}(\cdot, p)$ is the operator of resizing a 2D patch to the size of $p \times p$ with bicubic interpolation [25].

TABLE 3
Results on MNIST-rot-12k of competing methods with similar simple network architecture.

Method	Test Error(%)	Params
G-CNN [6]	2.74	189k
E2-CNN [4]	1.18	42k
PDO-eConv [5]	1.52	57k
F-Conv	1.15	95k

Fig. 6 shows an example of the representation results of (35) for the cases $p = 11$ and $p = 5$, respectively, where PDO based method is only tested on the case $p = 5$. In this experiment, although there is no ground truth for the rotation of the object filter, the performance of rotation can still be visually assessed through observation. For the case $p = 11$, it is easy to see that the filter representation result of harmonics bases is worse than other two comparison methods, where some sharp dark and bright pixels are evidently lost, also leading to a blurry effect of the rotation result. Meanwhile, the rotation result achieved by classical Fourier bases is obviously harmed by the fence effect, although its representation of the original input is exact. As comparison, the proposed method can achieve relatively better representation and rotation for a random filter initialized by (35). For the case of $p = 5$, one can also easily observe that the proposed method outperforms other competing methods. In particular, the filter representations of PDO and harmonics based method are more degenerated among all comparison methods, and the proposed method more faithfully preserves the local configurations (e.g., the black in the upper left and the deep gray in the upper right) after filter rotation.

Moreover, we repeat the experiments for 1000 times and calculate the relative-mean-square error (RMSE) of filter parametrization of each completing method. The results are shown in the last 2 columns of Table. 2. It is easy to observe that the 2D Fourier bases and proposed bases can both exactly represent the filter, and both evidently outperform the harmonic and PDO based filter parametrizations.

5.2 Experimental Results on Image Classification

MNIST-rot-12k [26] is the standard benchmark for rotation-equivariant models. It contains handwritten digits of the classical MNIST¹⁴, rotated by a random angle from 0 to 2π (full angle). The dataset contains 12,000 training samples and 50,000 test samples, respectively. Meanwhile, we randomly select 2,000 training images as a validation set and choose the model with the lowest validation error during training. Following [3], we augment the dataset with continuous rotations during the training progress.

Comparison in simple architectures. We first evaluate the performance of F-Conv with comparison to the current equivariant convolution methods. The competing methods include G-CNN [6], E2-CNN [4] and PDO-eConv [5], which are the most typical equivariant convolutions along this research line. Note that the last two methods are the state of the art filter parametrization based equivariant convolution methods. We use the same network architectures

TABLE 4
Results on MNIST-rot-12k of leading board methods and ours.

Method	Test Error(%)
H-Net [17]	1.69
OR-TIPooling [15]	1.54
RotEqNet [16]	1.09
PTN-CNN [12]	0.89
SFCNN [3]	0.714
E2-CNN [4]	0.716
PDO-eConv [5]	0.709
F-Conv	0.678

with convolutions replaced by the equivariant convolutions proposed in the competing methods.

We consider the $p8$ group for E2CNN, PDO-eConv and the proposed F-Conv methods, and exploit a CNN model with 6 convolutional layers and a fully connected layer, while the first convolutional layers have 7 channels and the other convolution layers are all set to be with 10 channels. Each convolutional layer consistently contains a convolution, a batch normalization and a ReLU operator. We exploit $p4$ group for G-CNN since it is designed for $p4$ groups, and we set double times of the filter number for GCNN in each network layer to make its channel number similar with other methods. The filter size of these competing methods is all set as 5. We use Adam optimizer [27] with a weight decay of 0.001 to train the networks for 100 epoches. The batch size is set to be 128. The learning rate is started with 10^{-3} and reduced gradually to 10^{-5} .

As shown in Table 3, with similar network architectures, the proposed F-Cov can achieve the lowest test error. The exploited parameter number of F-Conv is also with the same level to the state of the art methods along this line. In specific, the difference of these methods in parameter number is mainly attributed to their different basis numbers for representing a filter (E2CNN contains 11 bases, PDO-eConv contains 15 bases, F-Conv contains 25 bases).

Comparison with the leading board methods. We then compare the performance of our F-Conv with more competitive models. The competing method includes H-Net [17], OR-TIPooling [15], RotEqNet [16], PTN-CNN [12], SFCNN [3], E2-CNN [4] and PDO-eConv [5].

Following E2-CNN [4], we set the group size and filter size to be 12 and 5, respectively. The model is trained using the Adam algorithm [27] with a weight decay of 0.001. We train the network with the batch size 128 for 200 epoches. The initial learning rate is set as 5e-3 and reduced gradually to 5e-6, and the dropout rate is 0.25. We exploit a CNN model with 7 convolutional layers and a fully connected network. The convolutional layers have 16, 16, 32, 32, 32, 64 and 96 channels, respectively. Each convolutional layer of an F-Conv consistently includes a batch normalization, a ReLU and a dropout operator. We use spatial pooling and orientation pooling after the final F-Conv layer, and input the pooling result to the fully connected network, which contains 1 hidden layer, and the hidden nodes number is set to be 96.

Table 4 shows the results of F-Conv on MNIST-rot-12k, as well as the reported best results of leading board methods on this dataset. As shown in the table, the state of the art methods have achieved high precisions (e.g., 0.716%,

¹⁴<http://yann.lecun.com/exdb/mnist/>

0.714% and 0.709% test error for E2CNN, SFCNN and PDO-eConv, respectively). Comparatively, our method achieves 0.678% test error, getting further performance gain over the state of art methods. This substantiates the effectiveness of the propose F-Conv in this high-level task.

5.3 Experimental Results on Image Super-resolution

We then adopt the filter parameterized equivariant convolutions to a typical low-level image processing task, image super-resolution, for verifying their performance in low-level problems.

Single image super-resolution (SR), as a classical problem in computer vision, aims at recovering a high-resolution image from a single low-resolution image. Recently, deep convolutional neural network (CNN) based methods have achieved significant improvements over conventional SR methods [32], [33], [34], [35], [36], and attracted much research attention.

Network architecture settings. We exploit 3 state-of-the-art networks designs for SR tasks, including EDSR [32], RDN [33] and RCAN [34], for our experiments. The EDSR network consists of residual blocks [37], a global residual connection and an upsampling modular. In our experiments, we set the number of residual blocks to be 16, and set the channel number of each residual block to be 256. The RDN network consists of residual blocks [37], dense connections [38] and an upsampling modular. We set the number of residual blocks, the growth rate and conv number in RDN as 16, 64 and 8, respectively. The RCAN network consists of residual in residual (RIR) blocks and residual channel attention blocks. We set the number of RIR blocks, the number of residual blocks of RIR and the channel number of each residual block to be 10 and 16 and 64, respectively.

Convolutional method settings. The competing equivariant convolution methods include G-CNN [6], E2-CNN [4], PDO-eConv [5] and the proposed F-Conv. We replace the original convolutions in EDSR, RDN and RCAN with the competing convolutions, respectively.

For G-CNN based network, since an intermediate feature map is a 4-channel matrix, we set the channel number of residual blocks as $1/4$ of that in the original network, so as to make it to take similar memory as the original one. Following the original setting in EDSR, RDN and RCAN, the filter size is set as 3×3 in G-CNN based network. For E2-CNN, PDO-eConv and the proposed F-Conv, we exploit $p8$ group for the equivariant convolutions and set the channel number of each residual block (and the growth rate in RDN) as $1/8$ to the original networks in each layer to keep their similar memory with the original network. Besides, we set the filter size as 5×5 for these convolutions (this is due to that the PDO-eConv is only designed for filters with size 5×5 , and the circular shape masks in filters of E2CNN and F-Conv make 3×3 filters contain not sufficient effective pixels). Since the channel attention operation is not rotation equivariant, we remove the channel attention modular in the equivariant-convolution-based RCAN methods. It should be indicated that in these equivariant-convolution-based SR methods, the entire architecture of these networks are rotation equivariant except that the upsampling operator

at the tail parts of the networks. This does not substantially influence the effect brought by these rotation equivariant convolutions.

Datasets and degradation models. Following [32], [33], [34], we use 800 training images from DIV2K dataset [39] as the training set. For testing, we use four standard benchmark datasets, including Urban100 [28], B100 [29], Set14 [30] and Set5 [31], which contain 100, 100, 14 and 5 natural images, respectively. We conduct experiments with Bicubic (BI) and degradation models [32], [33], [34].

Training settings. For all competing methods in this series of experiments, we use Adam optimizer [27] with no weight decay to train the networks for 150 epoches. Besides, following the setting of the original paper of EDSR [32], RDN [33] and RCAN [34], during the training, we set the batch size for all the EDSR, RDN and RCAN based methods as 16. For the 2 scale super-resolution cases, we set the training patch size for EDSR, RDN and RCAN based methods as 96, 64 and 96, respectively, and set the training patch size for the 4 scale super-resolution cases double to the 2 scale cases. The initial leaning rate is set as 2×10^{-4} and then decreased to half at the 100 and 130 epoches.

Since the rotation-based data augmentation will lead to more “rotation equivariant” training results, and this effect may be mixed with the benefit resulted from rotation equivariant convolutions, we first train the competing methods without data augmentation, in order to observe the pure benefit from equivariant convolutions. Then, following the setting of previous methods, we also train the competing methods with randomly rotating the training images by 90° , 180° , 270° and flipping horizontally for data augmentation.

Quantitative results. Table 5 shows the SR results of the 15 competing methods on the 5 exploited data sets, without and with data augmentation, respectively. The evaluation measures include PSNR and SSIM [40] on Y channel (i.e., luminance) of the transformed YCbCr space. Comparing the results in Table 5, it is easy to observe that removing data augmentation will significantly degenerate the performance of the 3 CNN-based SR methods, especially in the 4 scale SR experiments. As comparison, the performance of equivariant-convolution-based methods does not change too much with or without data augmentation, since most of the network modulars in these methods are rotation equivariant. This phenomenon implies that the rotation symmetries of local features and rotation equivariant convolutions should be helpful for improving SR performance. Besides, one can also observe that E2-CNN and PDO-eConv method have not attained satisfactory SR performance, possibly due to their less representation accuracy of the filter parametrization methods. Comparatively, the proposed F-Conv method shows evident superiority than other filter-parametrization-based equivariant convolutions in this task, and achieves better result than CNN and G-CNN based methods which do not involve filter parametrization. To the best we known, this should be the first filter parametrization based rotation equivariant convolutions that can help intrinsically improve the performance of low-level tasks.

Visual results. Figs. 7-10 visually show the SR results of all competing methods on 2 samples from the Urban100 dataset, with SR scale set as 2, trained without augmentation, and SR scale set as 4, trained with data augmentation,

TABLE 5

The average testing results of all competing methods on the 4 exploited image datasets, including Urban100 [28], B100 [29], Set14 [30] and Set5 [31]. The results in the upper and lower parts of the table is produced by networks trained without and with data argumentation, respectively.

Method	argu.	x2						x4					
		EDSR [32]		RDN [33]		RCAN [34]		EDSR [32]		RDN [33]		RCAN [34]	
		PNSR	SSIM										
CNN	×	32.389	0.9175	32.383	0.9256	32.481	0.9185	26.949	0.7685	27.048	0.7711	27.023	0.7703
G-CNN [6]	×	32.439	0.9180	32.450	0.9180	32.565	0.9189	27.021	0.7695	27.078	0.7723	27.133	0.7737
E2-CNN [4]	×	32.232	0.9163	32.331	0.9169	32.009	0.9138	26.950	0.7675	27.034	0.7695	26.718	0.7602
PDO-eConv [5]	×	31.622	0.9088	31.406	0.9064	31.789	0.9108	26.555	0.7523	25.774	0.7255	26.553	0.7534
F-Conv	×	32.508	0.9184	32.604	0.9320	32.709	0.9203	27.146	0.7742	27.207	0.7756	27.208	0.7745
CNN	✓	32.439	0.9179	32.446	0.9180	32.521	0.9187	27.179	0.7740	27.200	0.7750	27.260	0.7764
G-CNN [6]	✓	32.459	0.9179	32.453	0.9181	32.567	0.9191	27.180	0.7747	27.096	0.7729	27.201	0.7749
E2-CNN [4]	✓	32.296	0.9167	32.361	0.9174	32.030	0.9138	26.953	0.7674	27.057	0.7707	26.768	0.7613
PDO-eConv [5]	✓	31.648	0.9090	30.763	0.8986	31.747	0.9104	26.590	0.7538	25.834	0.7277	26.510	0.7523
F-Conv	✓	32.519	0.9186	32.658	0.9202	32.730	0.9207	27.253	0.7764	27.265	0.7770	27.320	0.7784

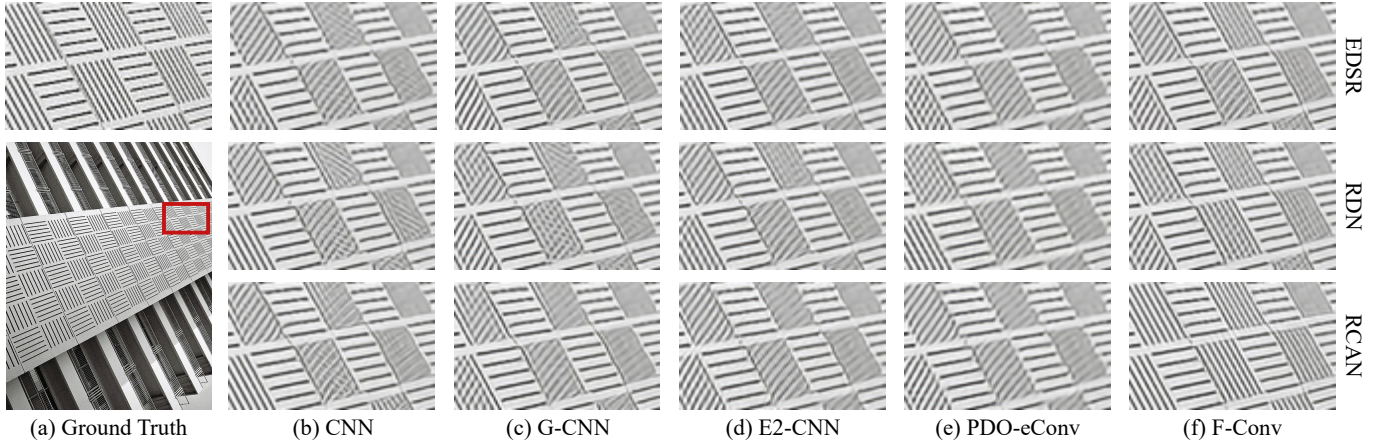


Fig. 7. (a) A sample of high-resolution image from the Urban100 [28] dataset. (b) From upper to lower: the 2 times super-resolution images restored by the EDSR, RDN and RCAN methods, respectively, where the convolution operators are set as commonly used convolutions, i.e., CNN. (c)-(f) From upper to lower: the super-resolution images restored by the EDSR, RDN and RCAN methods, respectively, where the convolution operators are set as G-CNN, E2-CNN, PDO-eConv and the proposed F-Conv, respectively. All the involved methods are trained without data argumentation.

respectively. From these figures, it is easy to observe that the SR results of filter parametrization based method like E2-CNN and PDO-eConv based methods are usually with over-smooth artifacts and certainly lose texture details. As comparison, F-Conv based method performs evidently better in sense of achieving clearer SR image and more faithfully preserving image textures and edges, which are superior to the methods based on other 4 convolutions. This implies that the proposed filter parametrization method should be helpful to enhance the performance of low-level computer vision tasks.

6 CONCLUSION

In this paper we have proposed a novel filter parametrization method, and built rotation equivariant convolutions basing on it. The proposed filter parametrization can be viewed as an enhanced version of Fourier series expansion, where we reduce the maximum frequency of the bases by exploiting symmetrical functions of low frequency Fourier bases to replace the high frequency ones. By theoretical analysis and empirical experiment evaluation, we have shown that the proposed filter parametrization method inherits the high-accuracy of Fourier series expansion for representing functional filter when there is no rotation, and

more importantly, it significantly alleviates the heavy fence effect which original Fourier series expansion suffers from. In this way, the proposed filter parametrization method evidently prompts the low-accuracy representation issue of previous filter parametrization methods. Based on the proposed filter parametrization, we construct a new equivariant convolution framework, named F-Conv, and analyze its theoretical properties in detail. We have further demonstrated the superiority of the proposed F-Conv beyond previous filter parametrization methods. Especially, to the best of our knowledge, F-Conv should be the first equivariant convolution that could intrinsically help evidently improve the performance of the low-level task (specifically, image super-resolution), implying its better preservation capability of the rotation symmetries (more than 4 angles) of image features, and potential usefulness for a wider range of image processing tasks.

Except rotation equivariant convolutions, a filter parametrization method with high accuracy should be useful for the designing of many other learnable operators in deep learning frameworks. In our future work, we will further extend the proposed filter parametrization methodology and explore more applications along this line. Typically, the multi-scale network modules play an important role in many computer vision tasks, and the proposed filter

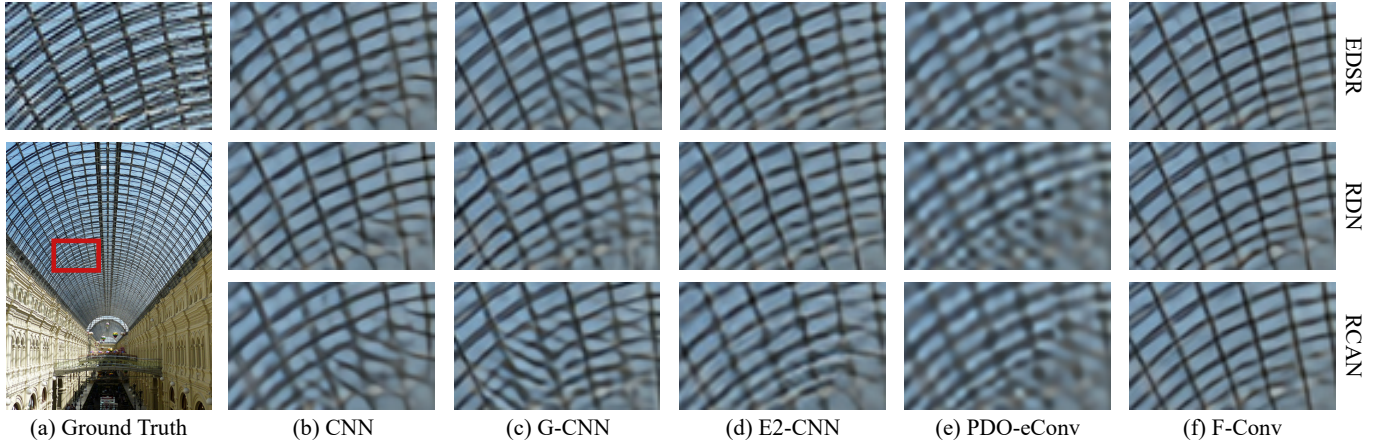


Fig. 8. (a) A sample of high-resolution image from the Urban100 [28] dataset. (b) From upper to lower: the 4 times super-resolution images restored by the EDSR, RDN and RCAN methods, respectively, where the convolution operators are set as commonly used convolutions, i.e., CNN. (c)-(f) From upper to lower: the super-resolution images restored by the EDSR, RDN and RCAN methods, respectively, where the convolution operators are set as G-CNN, E2-CNN, PDO-eConv and the proposed F-Conv, respectively. All the involved methods are trained without data augmentation.

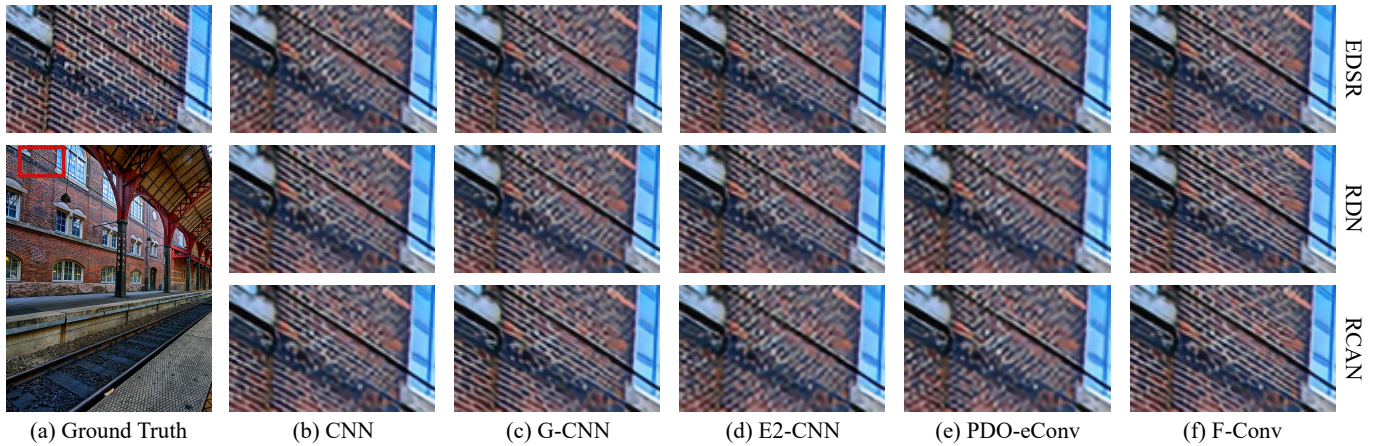


Fig. 9. (a) A sample of high-resolution image from the Urban100 [28] dataset. (b) From upper to lower: the 2 times super-resolution images restored by the EDSR, RDN and RCAN methods, respectively, where the convolution operators are set as commonly used convolutions, i.e., CNN. (c)-(f) From upper to lower: the super-resolution images restored by the EDSR, RDN and RCAN methods, respectively, where the convolution operators are set as G-CNN, E2-CNN, PDO-eConv and the proposed F-Conv, respectively. All the involved methods are trained with data augmentation.

parametrization framework is hopeful to be extended to design novel and rational multi-scale filters. A feasible strategy might be to discretize the functional filter with different resolutions, and then multi-scale filters with shared parameters can be obtained. Besides, multi-angle filters can be used to model the noise in low-dose computed tomography images, since this kind of domain noise shares similar patterns with different angles. Furthermore, the proposed parametrization strategy can also be used in dynamic network design, where one can input different kinds of transformations to a learnable filter to dynamically control the network.

REFERENCES

- [1] Matthew D Zeiler and Rob Fergus. Visualizing and understanding convolutional networks. In *European conference on computer vision*, pages 818–833. Springer, 2014.
- [2] Christian Szegedy, Wei Liu, Yangqing Jia, Pierre Sermanet, Scott Reed, Dragomir Anguelov, Dumitru Erhan, Vincent Vanhoucke, and Andrew Rabinovich. Going deeper with convolutions. In *Proceedings of the IEEE conference on computer vision and pattern recognition*, pages 1–9, 2015.
- [3] Maurice Weiler, Fred A Hamprecht, and Martin Storath. Learning steerable filters for rotation equivariant cnns. In *Proceedings of the IEEE Conference on Computer Vision and Pattern Recognition*, pages 849–858, 2018.
- [4] Maurice Weiler and Gabriele Cesa. General $e(2)$ -equivariant steerable cnns. 2019.
- [5] Zhengyang Shen, Lingshen He, Zhouchen Lin, and Jinwen Ma. Pdo-econvs: Partial differential operator based equivariant convolutions. In *International Conference on Machine Learning*, pages 8697–8706. PMLR, 2020.
- [6] Taco Cohen and Max Welling. Group equivariant convolutional networks. In *Proceedings of The 33rd International Conference on Machine Learning*, pages 2990–2999. PMLR, 2016.
- [7] Emiel Hoogeboom, Jorn W. T. Peters, Taco S. Cohen, and Max Welling. Hexaconv, 2018.
- [8] Soo-Chang Pei and Min-Hung Yeh. Two dimensional discrete fractional fourier transform. *Signal Processing*, 67(1):99–108, 1998.
- [9] William T Freeman, Edward H Adelson, et al. The design and use of steerable filters. *IEEE Transactions on Pattern analysis and machine intelligence*, 13(9):891–906, 1991.
- [10] Alex Krizhevsky, Ilya Sutskever, and Geoffrey E Hinton. Imagenet classification with deep convolutional neural networks. *Advances in neural information processing systems*, 25:1097–1105, 2012.
- [11] Dmitry Laptev, Nikolay Savinov, Joachim M Buhmann, and Marc Pollefeys. Ti-pooling: transformation-invariant pooling for feature learning in convolutional neural networks. In *Proceedings of the IEEE conference on computer vision and pattern recognition*, pages 289–297, 2016.
- [12] Carlos Esteves, Christine Allen-Blanchette, Xiaowei Zhou, and Kostas Daniilidis. Polar transformer networks. *arXiv preprint*

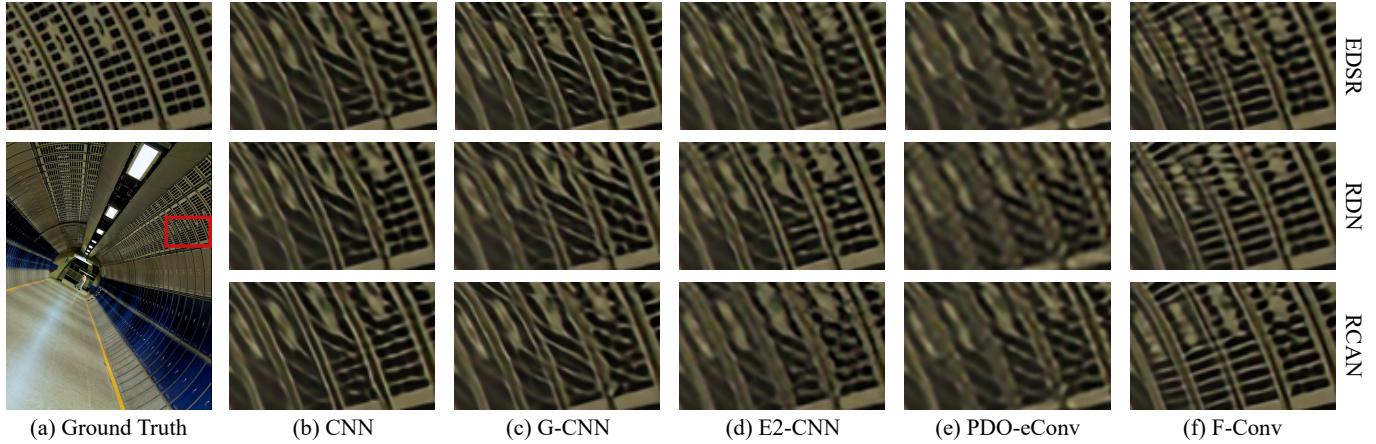


Fig. 10. (a) A sample of high resolution image from the Urban100 [28] dataset. (b) From upper to lower: the 4 times super-resolution images restored by the EDSR, RDN and RCAN methods, respectively, where the convolution operators are set as commonly used convolutions, i.e., CNN. (c)-(f) From upper to lower: the super-resolution images restored by the EDSR, RDN and RCAN methods, respectively, where the convolution operators are set as G-CNN, E2-CNN, PDO-eConv and the proposed F-Conv, respectively. All the involved methods are trained with data argumentation.

arXiv:1709.01889, 2017.

[13] Kihyuk Sohn and Honglak Lee. Learning invariant representations with local transformations. *arXiv preprint arXiv:1206.6418*, 2012.

[14] Kaiming He, Xiangyu Zhang, Shaoqing Ren, and Jian Sun. Delving deep into rectifiers: Surpassing human-level performance on imagenet classification. In *Proceedings of the IEEE international conference on computer vision*, pages 1026–1034, 2015.

[15] Yanzhao Zhou, Qixiang Ye, Qiang Qiu, and Jianbin Jiao. Oriented response networks. In *Proceedings of the IEEE Conference on Computer Vision and Pattern Recognition (CVPR)*, July 2017.

[16] Diego Marcos, Michele Volpi, Nikos Komodakis, and Devis Tuia. Rotation equivariant vector field networks. In *Proceedings of the IEEE International Conference on Computer Vision (ICCV)*, Oct 2017.

[17] Daniel E. Worrall, Stephan J. Garbin, Daniyar Turmukhambetov, and Gabriel J. Brostow. Harmonic networks: Deep translation and rotation equivariance. In *Proceedings of the IEEE Conference on Computer Vision and Pattern Recognition (CVPR)*, July 2017.

[18] Zhengyang Shen, Tiansheng Shen, Zhouchen Lin, and Jinwen Ma. Pdo-es 2 cnns: Partial differential operator based equivariant spherical cnns. *AAAI 2021*.

[19] Qi Xie, Qian Zhao, Zongben Xu, and DeYu Meng. Color and direction-invariant nonlocal self-similarity prior and its application to color image denoising. *Science China Information Sciences*, 63(12):1–17, 2020.

[20] E. Oran Brigham. *The fast fourier transform and its applications*. Prentice-Hall, Inc., 1988.

[21] Xavier Glorot and Yoshua Bengio. Understanding the difficulty of training deep feedforward neural networks. In *Proceedings of the Thirteenth International Conference on Artificial Intelligence and Statistics*, pages 249–256, 2010.

[22] Kaiming He, Xiangyu Zhang, Shaoqing Ren, and Jian Sun. Delving deep into rectifiers: Surpassing human-level performance on imagenet classification. In *Proceedings of the IEEE International Conference on Computer Vision (ICCV)*, December 2015.

[23] Boyd Stephen and Vandenberghe Lieven. *Convex optimization*. Cambridge university press, 2004.

[24] Shyh-Jier Huang, Cheng-Tao Hsieh, and Ching-Lien Huang. Application of morlet wavelets to supervise power system disturbances. *IEEE Transactions on Power Delivery*, 14(1):235–243, 1999.

[25] Dianyuan Han. Comparison of commonly used image interpolation methods. In *Proceedings of the 2nd International Conference on Computer Science and Electronics Engineering (ICCSEE 2013)*, pages 1556–1559, 2013/03.

[26] Hugo Larochelle, Dumitru Erhan, Aaron Courville, James Bergstra, and Yoshua Bengio. An empirical evaluation of deep architectures on problems with many factors of variation. In *Proceedings of the 24th International Conference on Machine Learning*, page 473–480, 2007.

[27] Jimmy Ba Diederik Kingma. Adam: A method for stochastic optimization. In *ICLR*, 2015.

[28] Jia-Bin Huang, Abhishek Singh, and Narendra Ahuja. Single image super-resolution from transformed self-exemplars. In *Proceedings of the IEEE conference on computer vision and pattern recognition*, pages 5197–5206, 2015.

[29] David Martin, Charless Fowlkes, Doron Tal, and Jitendra Malik. A database of human segmented natural images and its application to evaluating segmentation algorithms and measuring ecological statistics. In *Proceedings Eighth IEEE International Conference on Computer Vision. ICCV 2001*, volume 2, pages 416–423. IEEE, 2001.

[30] Roman Zeyde, Michael Elad, and Matan Protter. On single image scale-up using sparse-representations. In *International conference on curves and surfaces*, pages 711–730. Springer, 2010.

[31] Marco Bevilacqua, Aline Roumy, Christine Guillemot, and Marie Line Alberi-Morel. Low-complexity single-image super-resolution based on nonnegative neighbor embedding. 2012.

[32] Bee Lim, Sanghyun Son, Heewon Kim, Seungjun Nah, and Kyoung Mu Lee. Enhanced deep residual networks for single image super-resolution. In *Proceedings of the IEEE conference on computer vision and pattern recognition workshops*, pages 136–144, 2017.

[33] Yulun Zhang, Yapeng Tian, Yu Kong, Bineng Zhong, and Yun Fu. Residual dense network for image super-resolution. In *Proceedings of the IEEE conference on computer vision and pattern recognition*, pages 2472–2481, 2018.

[34] Yulun Zhang, Kunpeng Li, Kai Li, Lichen Wang, Bineng Zhong, and Yun Fu. Image super-resolution using very deep residual channel attention networks. In *Proceedings of the European conference on computer vision (ECCV)*, pages 286–301, 2018.

[35] Zhihao Wang, Jian Chen, and Steven CH Hoi. Deep learning for image super-resolution: A survey. *IEEE transactions on pattern analysis and machine intelligence*, 2020.

[36] Chao Dong, Chen Change Loy, Kaiming He, and Xiaoou Tang. Learning a deep convolutional network for image super-resolution. In *European conference on computer vision*, pages 184–199. Springer, 2014.

[37] Kaiming He, Xiangyu Zhang, Shaoqing Ren, and Jian Sun. Deep residual learning for image recognition. In *Proceedings of the IEEE conference on computer vision and pattern recognition*, pages 770–778, 2016.

[38] Gao Huang, Zhuang Liu, Laurens Van Der Maaten, and Kilian Q Weinberger. Densely connected convolutional networks. In *Proceedings of the IEEE conference on computer vision and pattern recognition*, pages 4700–4708, 2017.

[39] Radu Timofte, Eirikur Agustsson, Luc Van Gool, Ming-Hsuan Yang, and Lei Zhang. Ntire 2017 challenge on single image super-resolution: Methods and results. In *Proceedings of the IEEE conference on computer vision and pattern recognition workshops*, pages 114–125, 2017.

[40] Zhou Wang, Alan C Bovik, Hamid R Sheikh, and Eero P Simoncelli. Image quality assessment: from error visibility to structural similarity. *IEEE transactions on image processing*, 13(4):600–612, 2004.

“Fourier Series Expansion Based Filter Parametrization for Equivariant Convolutions”: Supplementary Material

Qi Xie, Qian Zhao, Zongben Xu and Deyu Meng

Abstract—In this supplementary material, we provide the proofs to main theorems of the main paper. Besides, more implementation details and more experimental results are also presented.

1 PROOF TO THEOREM 1

In this section, we present the proof to Theorem 1 of the main text, which is about the theoretical properties of the proposed bases for filter parametrization.

Notations. Firstly, let us review some necessary notations as defined in the main text. We denote the 2D Fourier bases (with a circular shape mask for better performing rotation) as follows:

$$\begin{aligned}\phi_{kl}^c(x) &= \Omega(x) \cos\left(\frac{2\pi}{ph}[k, l] \cdot \begin{bmatrix} x_1 \\ x_2 \end{bmatrix}\right), \\ \phi_{kl}^s(x) &= \Omega(x) \sin\left(\frac{2\pi}{ph}[k, l] \cdot \begin{bmatrix} x_1 \\ x_2 \end{bmatrix}\right),\end{aligned}\quad (1)$$

where $k, l = 0, 1, \dots, p-1$ and $\Omega(x) \geq 0$ is a radial mask function that equals to 0 when $\|x\| > (p+1)h/2$. Its definition will be introduced in Section 4 of this supplementary material for more description. We denote the proposed bases in following formulation:

$$\begin{aligned}\varphi_{kl}^c(x) &= \Omega(x) \cos\left(\frac{2\pi}{ph}[\mathcal{I}_p(k), \mathcal{I}_p(l)] \cdot \begin{bmatrix} x_1 \\ x_2 \end{bmatrix}\right), \\ \varphi_{kl}^s(x) &= \Omega(x) \sin\left(\frac{2\pi}{ph}[\mathcal{I}_p(k), \mathcal{I}_p(l)] \cdot \begin{bmatrix} x_1 \\ x_2 \end{bmatrix}\right),\end{aligned}\quad (2)$$

where $k, l = 0, 1, \dots, p-1$, $\Omega(x)$ is defined as Eq. (1), and for any integer m ,

$$\mathcal{I}_p(m) = \begin{cases} m & \text{if } m \leq p/2 \\ m-p & \text{if } m > p/2 \end{cases} \quad (3)$$

Then we can prove the following theorem:

Theorem 1. For any mesh size $h \in \mathbb{R}$, filter size $p \in \mathbb{N}_+$, and grid point x on the $p \times p$ mesh of $[(1-p)h/2, (p-1)h/2]^2$, i.e., $x_1 = (i - (p-1)/2)h$, $x_2 = (j - (p-1)/2)h$, $\forall i, j = 0, 1, \dots, p-1$, let $k, l = 0, 1, \dots, p-1$, then,

$$\begin{aligned}\varphi_{kl}^c(x) &= s(p, k, l) \cdot \phi_{kl}^c(x), \\ \varphi_{kl}^s(x) &= s(p, k, l) \cdot \phi_{kl}^s(x),\end{aligned}\quad (4)$$

where φ_{kl}^c and φ_{kl}^s are defined in Eq. (2), ϕ_{kl}^c , ϕ_{kl}^s are defined in Eq. (1), $s(p, k, l) \in \{-1, 1\}$, satisfying that $s(p, k, l) = \text{sign}(k - p/2 + \epsilon)^{p-1} \cdot \text{sign}(l - p/2 + \epsilon)^{p-1}$, $0 < \epsilon < 1/2$.

Qi Xie, Qian Zhao, Zongben Xu and Deyu Meng (corresponding author) are with School of Mathematics and Statistics and Ministry of Education Key Lab of Intelligent Networks and Network Security, Xi'an Jiaotong University, Shaanxi, P.R.China.

Email: {xie.qi, timmy.zhaqian, zbxu, dymeng}@mail.xjtu.edu.cn

Proof. 1) When p is an odd number, then

$$\begin{aligned}x_1 &= \left(i - \frac{(p-1)}{2}\right)h = mh, \quad \forall m, n \in \mathbb{N} \\ x_2 &= \left(j - \frac{(p-1)}{2}\right)h = nh, \quad \forall m, n \in \mathbb{N}.\end{aligned}\quad (5)$$

In this case, $s(p, k, l) = 1$.

a) If $k \leq p/2$ and $l \leq p/2$, $\mathcal{I}_p(k) = k$, and $\mathcal{I}_p(l) = l$, obviously, (4) is satisfied.

b) If $k \leq p/2$ and $l > p/2$, then $\mathcal{I}_p(k) = k$, and $\mathcal{I}_p(l) = l - p$, and we can obtain

$$\begin{aligned}\varphi_{kl}^c(x) &= \Omega(x) \cos\left(\frac{2\pi}{ph}(kx_1 + (l-p)x_2)\right) \\ &= \Omega(x) \cos\left(\frac{2\pi}{ph}(kx_1 + lx_2) - \frac{2\pi}{ph} \cdot p \cdot x_2\right) \\ &= \Omega(x) \cos\left(\frac{2\pi}{ph}(kx_1 + lx_2) - 2n\pi\right) \\ &= \Omega(x) \cos\left(\frac{2\pi}{ph}(kx_1 + lx_2)\right) = \phi_{kl}^c(x).\end{aligned}\quad (6)$$

Obviously, we can prove that $\varphi_{kl}^s(x) = \phi_{kl}^s(x)$ in the similar way.

c) If $k > p/2$ and $l \leq p/2$, then the result can be proved similarly as (b).

d) If $k > p/2$ and $l > p/2$, then $\mathcal{I}_p(k) = k - p$, and $\mathcal{I}_p(l) = l - p$, and we can obtain

$$\begin{aligned}\varphi_{kl}^c(x) &= \Omega(x) \cos\left(\frac{2\pi}{ph}((k-p)x_1 + (l-p)x_2)\right) \\ &= \Omega(x) \cos\left(\frac{2\pi}{ph}(kx_1 + lx_2) - \frac{2\pi}{ph} \cdot p \cdot (x_1 + x_2)\right) \\ &= \Omega(x) \cos\left(\frac{2\pi}{ph}(kx_1 + lx_2) - 2(m+n)\pi\right) \\ &= \Omega(x) \cos\left(\frac{2\pi}{ph}(kx_1 + lx_2)\right) = \phi_{kl}^c(x).\end{aligned}\quad (7)$$

Obviously, the equation $\varphi_{kl}^s(x) = \phi_{kl}^s(x)$ can be proved in the similar way.

2) When p is an even number, then

$$\begin{aligned} x_1 &= \left(i - \frac{(p-1)}{2} \right) h = \left(m + \frac{1}{2} \right) h, \forall m, n \in \mathbb{N} \\ x_2 &= \left(j - \frac{(p-1)}{2} \right) h = \left(m + \frac{1}{2} \right) h, \forall m, n \in \mathbb{N}. \end{aligned} \quad (8)$$

a) If $k \leq p/2$ and $l \leq p/2$, $\mathcal{I}_p(k) = k$, $\mathcal{I}_p(l) = l$, $s(p, k, l) = 1$, Eq. (4) is obviously satisfied.

b) If $k \leq p/2$ and $l > p/2$, then $\mathcal{I}_p(k) = k$, $\mathcal{I}_p(l) = l - p$, and $s(p, k, l) = -1$, we can obtain

$$\begin{aligned} \varphi_{kl}^c(x) &= \Omega(x) \cos \left(\frac{2\pi}{ph} (kx_1 + (l-p)x_2) \right) \\ &= \Omega(x) \cos \left(\frac{2\pi}{ph} (kx_1 + lx_2) - \frac{2\pi}{ph} \cdot p \cdot x_2 \right) \\ &= \Omega(x) \cos \left(\frac{2\pi}{ph} (kx_1 + lx_2) - (2n+1)\pi \right) \\ &= -\Omega(x) \cos \left(\frac{2\pi}{ph} (kx_1 + lx_2) \right) = -\phi_{kl}^c(x). \end{aligned} \quad (9)$$

Obviously, the equation $\varphi_{kl}^s(x) = -\phi_{kl}^s(x)$ can then be proved in the similar way.

c) If $k > p/2$ and $l \leq p/2$, then the result can be proved similarly as (b).

d) If $k > p/2$ and $l > p/2$, then $\mathcal{I}_p(k) = k - p$, $\mathcal{I}_p(l) = l - p$ and $s(p, k, l) = 1$, and we can obtain

$$\begin{aligned} \varphi_{kl}^c(x) &= \Omega(x) \cos \left(\frac{2\pi}{ph} ((k-p)x_1 + (l-p)x_2) \right) \\ &= \Omega(x) \cos \left(\frac{2\pi}{ph} (kx_1 + lx_2) - \frac{2\pi}{ph} \cdot p \cdot (x_1 + x_2) \right) \\ &= \Omega(x) \cos \left(\frac{2\pi}{ph} (kx_1 + lx_2) - 2(m+n+1)\pi \right) \\ &= \Omega(x) \cos \left(\frac{2\pi}{ph} (kx_1 + lx_2) \right) = \phi_{kl}^c(x). \end{aligned} \quad (10)$$

Obviously, the equation $\varphi_{kl}^s(x) = \phi_{kl}^s(x)$ can be proved in the similar way. \square

2 PROOFS TO THEOREM 2 AND 3

Theorem 2 and Theorem 3 are about the error analysis to the proposed equivariant convolutions. It is worth mentioning that the idea of providing these error analysis is inspired by the theoretical results in [1]. In Theorem 2 we prove that the equivariance of the proposed equivariant convolutions are exact in continuous domain, just as the PDO-eConv did in [1]. In Theorem 3, we prove that for the proposed F-Conv, the error bound (for discrete cases) is related to the mesh size h in the same way as the theoretical results in [1], which is $O(h^2)$.

However, since the definition of the proposed F-Conv is very different from PDO-eConv in [1], totally different proofs for the two theorems are demanded here, which are actually evidently more complex than those ones in [1]. Besides, since the filter size p of F-Conv can be changed (while the filter size in PDO-eConv is fixed as 5), the error bound of our F-Conv is also with respect to p in the discrete cases, which is also very different from PDO-eConv. All these variations make the proofs of these look-like similar theoretical results more difficult than those provided in [1].

2.1 Proof to Theorem 2

Notations. For an input $r \in C^\infty(\mathbb{R}^2)$ and transformation $\tilde{A} \in O(2)$, \tilde{A} act on r by

$$\pi_{\tilde{A}}^R[r](x) = r(\tilde{A}^{-1}x), \forall x \in \mathbb{R}^2. \quad (11)$$

For a feature map $e \in C^\infty(E(2))$ and transformation $\tilde{A} \in O(2)$, \tilde{A} act on e by

$$\pi_{\tilde{A}}^E[e](x, A) = e(\tilde{A}^{-1}x, \tilde{A}^{-1}A), \forall (x, A) \in E(2). \quad (12)$$

Ψ denotes the convolution on input layer, which maps an input $r \in C^\infty(\mathbb{R}^2)$ to a feature map defined on $E(2)$:

$$\Psi[r](y, A) = \int_{\mathbb{R}^2} \varphi_{in}(A^{-1}x) r(y-x) d\sigma(x), \quad (13)$$

for any $(y, A) \in E(2)$, where σ is a measure imposed on \mathbb{R}^2 and φ_{in} is the proposed parameterized filter. Φ denotes the convolution on the intermediate layer, which maps a feature map $e \in C^\infty(E(2))$ to another feature map defined on $E(2)$:

$$\Phi[e](y, B) = \int_{\mathbb{R}^2} \int_{O(2)} \varphi_A(B^{-1}x) e(y-x, BA) d\sigma(x) dv(A), \quad (14)$$

for any $(y, B) \in E(2)$, where v is a measure on $O(2)$, $A, B \in O(2)$ denote orthogonal transformations in the considered group, and $\varphi_{\tilde{A}}$ indicates the filter with respect to the channel of feature map indexed by \tilde{A} , i.e., $e(x, A)|_{A=\tilde{A}}$. Υ represents the convolution on the final layer, which maps a feature map $e \in C^\infty(E(2))$ to a function defined on \mathbb{R}^2 . That is, for any $y \in \mathbb{R}^2$:

$$\Upsilon[e](y) = \int_{\mathbb{R}^2} \int_{O(2)} \varphi_{out}(B^{-1}x) e(y-x, B) d\sigma(x) dv(B), \quad (15)$$

Then we can prove the following theorem:

Theorem 2. For $r \in C^\infty(\mathbb{R}^2)$, $e \in C^\infty(E(2))$ and $\tilde{A} \in O(2)$, the following rules are satisfied:

$$\begin{aligned} \Psi \left[\pi_{\tilde{A}}^R[r] \right] &= \pi_{\tilde{A}}^E [\Psi[r]], \\ \Phi \left[\pi_{\tilde{A}}^E[e] \right] &= \pi_{\tilde{A}}^E [\Phi[e]], \\ \Upsilon \left[\pi_{\tilde{A}}^E[e] \right] &= \pi_{\tilde{A}}^R [\Upsilon[e]], \end{aligned} \quad (16)$$

where $\pi_{\tilde{A}}^R$, $\pi_{\tilde{A}}^E$, Ψ , Φ and Υ are defined by (11), (12), (13), (14) and (15), respectively.

Proof. (1) For any $y \in \mathbb{R}^2$ and $A \in O(2)$, we have

$$\begin{aligned} &\Psi \left[\pi_{\tilde{A}}^R[r] \right] (y, A) \\ &= \int_{\mathbb{R}^2} \varphi_{in}(A^{-1}x) \pi_{\tilde{A}}^R[r](y-x) d\sigma(x) \\ &= \int_{\mathbb{R}^2} \varphi_{in}(A^{-1}x) r(\tilde{A}^{-1}(y-x)) d\sigma(x). \end{aligned} \quad (17)$$

Let $\hat{x} = \tilde{A}^{-1}x$, since $|\det(\tilde{A})| = 1$, it holds that

$$\begin{aligned} &\int_{\mathbb{R}^2} \varphi_{in}(A^{-1}x) r(\tilde{A}^{-1}(y-x)) d\sigma(x), \\ &= \int_{\mathbb{R}^2} \varphi_{in} \left(\left(\tilde{A}^{-1}A \right)^{-1} \hat{x} \right) r(\tilde{A}^{-1}y - \hat{x}) d\sigma(\hat{x}) \\ &= \Psi[r](\tilde{A}^{-1}y, \tilde{A}^{-1}A) \\ &= \pi_{\tilde{A}}^E [\Psi[r]](y, A). \end{aligned} \quad (18)$$

This proves that $\Psi \left[\pi_{\tilde{A}}^R [r] \right] = \pi_{\tilde{A}}^E [\Psi [r]]$.

(2) Similar to the above proof in (1), for any $y \in \mathbb{R}^2$ and $B \in O(2)$, we can obtain that

$$\begin{aligned} & \Phi \left[\pi_{\tilde{A}}^E [e] \right] (y, B) \\ &= \int_{\mathbb{R}^2} \int_{O(2)} \varphi_A (B^{-1}x) \pi_{\tilde{A}}^E [e] (y - x, BA) d\sigma(x) v(A) \\ &= \int_{\mathbb{R}^2} \int_{O(2)} \varphi_A (B^{-1}x) \\ & \quad e(\tilde{A}^{-1}(y - x), \tilde{A}^{-1}BA) d\sigma(x) v(A) \quad (19) \\ &= \int_{\mathbb{R}^2} \int_{O(2)} \varphi_A \left((\tilde{A}^{-1}B)^{-1} \hat{x} \right) \\ & \quad e(\tilde{A}^{-1}y - \hat{x}, \tilde{A}^{-1}BA) d\sigma(x) v(A) \\ &= \Phi [e] (\tilde{A}^{-1}y, \tilde{A}^{-1}B) \\ &= \pi_{\tilde{A}}^E [\Phi [e]] (y, B). \end{aligned}$$

(3) For any $y \in \mathbb{R}^2$, we can deduce that

$$\begin{aligned} & \Upsilon \left[\pi_{\tilde{A}}^E [e] \right] (y) \\ &= \int_{\mathbb{R}^2} \int_{O(2)} \varphi_{out} (B^{-1}x) \pi_{\tilde{A}}^E [e] (y - x, B) d\sigma(x) v(B) \\ &= \int_{\mathbb{R}^2} \int_{O(2)} \varphi_{out} (B^{-1}x) \\ & \quad e(\tilde{A}^{-1}(y - x), \tilde{A}^{-1}B) d\sigma(x) v(B) \quad (20) \\ &= \int_{\mathbb{R}^2} \int_{O(2)} \varphi_{out} \left((\tilde{A}^{-1}B)^{-1} \hat{x} \right) \\ & \quad e(\tilde{A}^{-1}y - \hat{x}, \tilde{A}^{-1}B) d\sigma(x) v(B). \end{aligned}$$

Let $C = \tilde{A}^{-1}B$, and then we have

$$\begin{aligned} & \int_{\mathbb{R}^2} \int_{O(2)} \varphi_{out} \left((\tilde{A}^{-1}B)^{-1} \hat{x} \right) \\ & \quad e(\tilde{A}^{-1}y - \hat{x}, \tilde{A}^{-1}B) d\sigma(x) v(B) \\ &= \int_{\mathbb{R}^2} \int_{O(2)} \varphi_{out} (C^{-1}\hat{x}) \\ & \quad e(\tilde{A}^{-1}y - \hat{x}, C) d\sigma(x) v(C) \quad (21) \\ &= \Upsilon [e] (\tilde{A}^{-1}y) \\ &= \pi_{\tilde{A}}^R [\Upsilon [e]] (y). \end{aligned}$$

It can then be proved that $\Upsilon \left[\pi_{\tilde{A}}^E [r] \right] = \pi_{\tilde{A}}^R [\Upsilon [r]]$. \square

2.2 Proof to Theorem 3

Notations. We assume that an image $I \in R^{n \times n}$ represents a two-dimensional grid function obtained by discretizing a smooth function, i.e., for $i, j = 1, 2, \dots, n$,

$$I_{ij} = r(x_{ij}), \quad (22)$$

where $x_{ij} = ((i - \frac{n+1}{2})h, (j - \frac{n+1}{2})h)^T$. We represent F as a three-dimensional grid function sampled from a smooth function $e : \mathbb{R}^2 \times S \rightarrow \mathbb{R}$, and satisfying that for $i, j = 1, 2, \dots, n$,

$$F_{ij}^A = e(x_{ij}, A), \quad (23)$$

where $x_{ij} = ((i - \frac{n+1}{2})h, (j - \frac{n+1}{2})h)^T$ and $A \in S$, S is a subgroup of $O(2)$. For $i, j = 1, 2, \dots, p$, and $A, B \in S$,

$$\begin{aligned} \tilde{\Psi}_{ij}^A &= \varphi_{in} (A^{-1}x_{ij}), \\ \tilde{\Phi}_{ij}^{B,A} &= \varphi_A (B^{-1}x_{ij}), \\ \tilde{\Upsilon}_{ij}^A &= \varphi_{out} (A^{-1}x_{ij}), \end{aligned} \quad (24)$$

where $x_{ij} = ((i - (p+1)/2)h, (j - (p+1)/2)h)^T$, φ_{in} , φ_{out} and φ_A represent parametrized filters.

Let

$$\begin{aligned} x_{ij} &= \left(\left(i - \frac{p+1}{2} \right)h, \left(j - \frac{p+1}{2} \right)h \right)^T, \\ y_{ij} &= \left(\left(i - \frac{n+p+2}{2} \right)h, \left(j - \frac{n+p+2}{2} \right)h \right)^T. \end{aligned} \quad (25)$$

For any $A \in S$ and $i, j = 1, 2, \dots, n$, the convolution of $\tilde{\Psi}$ and I can be computed by

$$\begin{aligned} \left(\tilde{\Psi} \star I \right)_{ij}^A &= \sum_{(\tilde{i}, \tilde{j}) \in \Lambda} \varphi_{in} (A^{-1}x_{\tilde{i}\tilde{j}}) r(y_{ij} - x_{\tilde{i}\tilde{j}}) \\ &= \sum_{(\tilde{i}, \tilde{j}) \in \Lambda} \tilde{\Psi}_{\tilde{i}\tilde{j}}^A I_{i-\tilde{i}, j-\tilde{j}}, \end{aligned} \quad (26)$$

where Λ is a set of indexes, denoted as $\Lambda = \{(i, j) | i, j = 1, 2, \dots, p\}$, and $*$ is the common 2D convolution. For any $B \in S$ and $i, j = 1, 2, \dots, n$, the convolution of $\tilde{\Phi}$ and F is

$$\begin{aligned} \left(\tilde{\Phi} \star F \right)_{ij}^B &= \sum_{(\tilde{i}, \tilde{j}) \in \Lambda, A \in S} \varphi_A (B^{-1}x_{\tilde{i}\tilde{j}}) e(y_{ij} - x_{\tilde{i}\tilde{j}}, BA) \\ &= \sum_{(\tilde{i}, \tilde{j}) \in \Lambda, A \in S} \tilde{\Phi}_{\tilde{i}\tilde{j}}^{B,A} F_{i-\tilde{i}, j-\tilde{j}}^{BA}, \end{aligned} \quad (27)$$

where $\Lambda = \{(i, j) | i, j = 1, 2, \dots, p\}$. For $i, j = 1, 2, \dots, n$, the convolution of $\tilde{\Upsilon}$ and F is

$$\begin{aligned} \left(\tilde{\Upsilon} \star F \right)_{ij} &= \sum_{(\tilde{i}, \tilde{j}) \in \Lambda, B \in S} \varphi_{out} (B^{-1}x_{\tilde{i}\tilde{j}}) e(y_{ij} - x_{\tilde{i}\tilde{j}}, B) \\ &= \sum_{(\tilde{i}, \tilde{j}) \in \Lambda, B \in S} \tilde{\Upsilon}_{\tilde{i}\tilde{j}}^B F_{i-\tilde{i}, j-\tilde{j}}^B, \end{aligned} \quad (28)$$

where $\Lambda = \{(i, j) | i, j = 1, 2, \dots, p\}$. The transformations on I and F are defined by

$$\begin{aligned} \left(\tilde{\pi}_{\tilde{A}}^R (I) \right)_{ij} &= \pi_{\tilde{A}}^R [r](x_{ij}), \\ \left(\tilde{\pi}_{\tilde{A}}^E (F) \right)_{ij}^A &= \pi_{\tilde{A}}^E [e](x_{ij}, A), \\ \forall i, j &= 1, 2, \dots, n, \forall A, \tilde{A} \in S. \end{aligned} \quad (29)$$

Then we can prove the following lemmas.

Lemma 1. For smooth functions $r : \mathbb{R}^2 \rightarrow \mathbb{R}$ and $\varphi : \mathbb{R}^2 \rightarrow \mathbb{R}$, let $f(x) = \varphi(\tilde{A}^{-1}x) r(y - x)$. If for $x \in \mathbb{R}^2$, the following conditions are satisfied:

$$\begin{aligned} |r(x)| &\leq F_1, |\varphi(x)| \leq F_2, \\ \|\nabla r(x)\| &\leq G_1, \|\nabla \varphi(x)\| \leq G_2, \\ \|\nabla^2 r(x)\| &\leq H_1, \|\nabla^2 \varphi(x)\| \leq H_2, \\ \forall \|x\| &\geq (p+1/2)h, \varphi(x) = 0 \end{aligned} \quad (30)$$

where $p, h > 0$, ∇ and ∇^2 denote the operators of gradient and Hessian matrix, respectively, then $\forall \tilde{A} \in S, y \in \mathbb{R}$, the following rules are satisfied:

$$\begin{aligned} \max \left\{ \left| \frac{\partial^2 f(x)}{\partial x_1^2} \right|, \left| \frac{\partial^2 f(x)}{\partial x_2^2} \right| \right\} &\leq C, \\ \max \left\{ \left| \frac{d^2}{dx_2^2} \int_{\mathbb{R}} f(x) dx_1 \right|, \left| \frac{d^2}{dx_1^2} \int_{\mathbb{R}} f(x) dx_2 \right| \right\} &\leq C(p+1)h, \end{aligned} \quad (31)$$

where $C = F_1 H_2 + F_2 H_1 + 2G_1 G_2$.

Proof. It is easy to deduce that:

$$\begin{aligned} \left| \frac{\partial r(\tilde{A}y - x)}{\partial x_1} \right| &\leq \|\nabla r(x)\| \leq G_1, \\ \left| \frac{\partial \varphi(\tilde{A}x)}{\partial x_1} \right| &\leq \|\nabla \varphi(x)\| \leq G_2 \\ \left| \frac{\partial^2 r(\tilde{A}y - x)}{\partial x_1^2} \right| &\leq \|\nabla^2 r(x)\| \leq H_1, \\ \left| \frac{\partial^2 \varphi(\tilde{A}x)}{\partial x_1^2} \right| &\leq \|\nabla^2 \varphi(x)\| \leq H_2. \end{aligned} \quad (32)$$

Then we can obtain that

$$\begin{aligned} \left| \frac{\partial^2 f(x)}{\partial x_1^2} \right| &= \left| \frac{\partial \left(\varphi(\tilde{A}x) \partial r(y-x) + r(y-x) \partial \varphi(\tilde{A}x) \right)}{\partial x_1^2} \right| \\ &= \left| \frac{\varphi(\tilde{A}x) \partial^2 r(y-x) + r(y-x) \partial^2 \varphi(\tilde{A}x) + 2\partial \varphi(\tilde{A}x) \partial r(y-x)}{\partial x_1^2} \right| \\ &\leq F_1 H_2 + F_2 H_1 + 2G_1 G_2. \end{aligned} \quad (33)$$

Since the same result can be deduced for x_2 , this completes the proof of the first inequality.

Besides, $\forall \|x\| \geq (p+1/2)h$, $\varphi(x) = 0$. Only in the circular area with radius $(p+1/2)h$, we have $\left| \frac{\partial^2 f(x)}{\partial x_2^2} \right| > 0$. Therefore, it holds that

$$\begin{aligned} \left| \frac{d^2}{dx_2^2} \int_{\mathbb{R}} f(x) dx_1 \right| &= \left| \int_{\mathbb{R}} \frac{\partial^2}{\partial x_2^2} f(x) dx_1 \right| \\ &\leq \int_{-\frac{p+1}{2}h}^{\frac{p+1}{2}h} \left| \frac{\partial^2}{\partial x_2^2} f(x) \right| dx_1 \\ &\leq C(p+1)h. \end{aligned} \quad (34)$$

Since the same result can be deduced for x_2 , the proof can then be completed. \square

Lemma 2. For any $f : \mathbb{R} \rightarrow \mathbb{R}$, denote l as the linear interpolation function between points $x = a$ and $x = b$, i.e.,

$$l(x) = \frac{(x-a)f(b) + (b-x)f(a)}{b-a}. \quad (35)$$

If f'' is continuous in $[a, b]$ and $|f''(x)| \leq C$, then

$$|f(x) - l(x)| \leq \frac{C}{8}(a-b)^2. \quad (36)$$

Proof. Based on the Taylor's theorem with Lagrange remainder, we can obtain that

$$\begin{aligned} f(a) &= f(x) + (a-x)f'(x) + \frac{1}{2}(a-x)^2 f''(\xi) \\ f(b) &= f(x) + (b-x)f'(x) + \frac{1}{2}(b-x)^2 f''(\zeta). \end{aligned} \quad (37)$$

Besides, it is easy to deduce that

$$f(x) = \frac{(x-a)f(x) + (b-x)f(x)}{b-a}. \quad (38)$$

Thus,

$$\begin{aligned} &\frac{l(x) - f(x)}{b-a} \\ &= \frac{(x-a)(f(b) - f(x)) + (b-x)(f(a) - f(x))}{b-a} \\ &= (x-a) \left(\frac{1}{2}(b-x)^2 f''(\zeta) \right) + \\ &\quad (b-x) \left(\frac{1}{2}(a-x)^2 f''(\xi) \right) \\ &= \frac{(x-a)(b-x)}{2} \left(\frac{b-x}{b-a} f''(\zeta) + \frac{x-a}{b-a} f''(\xi) \right). \end{aligned} \quad (39)$$

Since $|(x-a)(b-x)| \leq (b-a)^2/4$, we can obtain

$$\begin{aligned} &|l(x) - f(x)| \\ &= \left| \frac{(x-a)(b-x)}{2} \left(\frac{b-x}{b-a} f''(\zeta) + \frac{x-a}{b-a} f''(\xi) \right) \right| \\ &\leq \left| \frac{(b-a)^2}{2} \left(\frac{b-x}{b-a} C + \frac{x-a}{b-a} C \right) \right| \\ &= \frac{C}{8}(b-a)^2. \end{aligned} \quad (40)$$

\square

Lemma 3. For smooth functions $r : \mathbb{R}^2 \rightarrow \mathbb{R}$ and $\varphi : \mathbb{R}^2 \rightarrow \mathbb{R}$, if for $x \in \mathbb{R}^2$, the following conditions are satisfied:

$$\begin{aligned} &|r(x)| \leq F_1, |\varphi(x)| \leq F_2, \\ &\|\nabla r(x)\| \leq G_1, \|\nabla \varphi(x)\| \leq G_2, \\ &\|\nabla^2 r(x)\| \leq H_1, \|\nabla^2 \varphi(x)\| \leq H_2, \\ &\forall \|x\| \geq (p+1/2)h, \varphi(x) = 0, \end{aligned} \quad (41)$$

where $p, h > 0$, ∇ and ∇^2 denote the operators of gradient and Hessian matrix, respectively, then $\forall \tilde{A} \in S, y \in \mathbb{R}$, the following rules are satisfied:

$$\begin{aligned} &\left| \int_{R^2} \varphi(\tilde{A}^{-1}x) r(y-x) d\sigma(x) - \right. \\ &\quad \left. \sum_{i,j \in \Lambda} \varphi(\tilde{A}^{-1}x_{ij}) r(y-x_{ij}) h^2 \right| \leq \frac{(p+1)^2 C}{4} h^4, \end{aligned} \quad (42)$$

where $A \in S$ and $\Lambda = \{(i,j) | i, j = 1, 2, \dots, p\}$, $x_{ij} = ((i-(p+1)/2)h, (j-(p+1)/2)h)^T$ and $C = F_1 H_2 + F_2 H_1 + 2G_1 G_2$.

Proof. 1) Denote $f(x) = \varphi(\tilde{A}^{-1}x) r(y-x)$, and we can prove that for any $n \in \mathbb{Z}$, it holds that

$$\left| \int_{\mathbb{R}} f \left(\begin{bmatrix} x_1 \\ nh \end{bmatrix} \right) dx_1 - \sum_{m \in \mathbb{Z}} f \left(\begin{bmatrix} mh \\ nh \end{bmatrix} \right) h \right| \leq \frac{C(p+1)}{8} h^3. \quad (43)$$

By Lemma 1, we can obtain that $\left| \frac{\partial^2 f(x)}{\partial x_1^2} \right| \leq C$. Then by Lemma 2, we can obtain that $\forall m, n \in \mathbb{Z}, mh \leq x_1 < (m+1)h$, it holds that

$$\left| f \left(\begin{bmatrix} x_1 \\ nh \end{bmatrix} \right) - l_{mn} \left(\begin{bmatrix} x_1 \\ nh \end{bmatrix} \right) \right| \leq \frac{C}{8} h^2, \quad (44)$$

where l_{mn} is the linear interpolation function of f between points $x = \begin{bmatrix} mh \\ nh \end{bmatrix}$ and $x = \begin{bmatrix} mh+h \\ nh \end{bmatrix}$, i.e.,

$$l_{mn}(x) = \frac{(x_1 - mh)f\left(\begin{bmatrix} mh+h \\ nh \end{bmatrix}\right) + (mh + h - x_1)f\left(\begin{bmatrix} mh \\ nh \end{bmatrix}\right)}{h}. \quad (45)$$

Thus,

$$\begin{aligned} & \left| \int_{mh}^{mh+h} \left(f\left(\begin{bmatrix} x_1 \\ nh \end{bmatrix}\right) \right) dx_1 - \int_{mh}^{mh+h} \left(l_{mn}\left(\begin{bmatrix} x_1 \\ nh \end{bmatrix}\right) \right) dx_1 \right| \\ &= \left| \int_{mh}^{mh+h} \left(f\left(\begin{bmatrix} x_1 \\ nh \end{bmatrix}\right) - l_{mn}\left(\begin{bmatrix} x_1 \\ nh \end{bmatrix}\right) \right) dx_1 \right| \\ &\leq \int_{mh}^{mh+h} \left| f\left(\begin{bmatrix} x_1 \\ nh \end{bmatrix}\right) - l_{mn}\left(\begin{bmatrix} x_1 \\ nh \end{bmatrix}\right) \right| dx_1 \\ &\leq \int_{mh}^{mh+h} \frac{C}{8} h^2 dx_1 = \frac{C}{8} h^3. \end{aligned} \quad (46)$$

Besides, we have

$$\begin{aligned} & \left| \int_{\mathbb{R}} f\left(\begin{bmatrix} x_1 \\ nh \end{bmatrix}\right) dx_1 - \sum_{m \in \mathbb{Z}} f\left(\begin{bmatrix} mh \\ nh \end{bmatrix}\right) h \right| \\ &= \left| \int_{\mathbb{R}} f\left(\begin{bmatrix} x_1 \\ nh \end{bmatrix}\right) dx_1 - \sum_{m \in \mathbb{Z}} \frac{h}{2} \left(f\left(\begin{bmatrix} mh \\ nh \end{bmatrix}\right) + f\left(\begin{bmatrix} mh+h \\ nh \end{bmatrix}\right) \right) \right| \\ &= \left| \int_{\mathbb{R}} f\left(\begin{bmatrix} x_1 \\ nh \end{bmatrix}\right) dx_1 - \sum_{m \in \mathbb{Z}} \int_{mh}^{mh+h} \left(l_{mn}\left(\begin{bmatrix} x_1 \\ nh \end{bmatrix}\right) \right) dx_1 \right| \\ &\leq \sum_{m \in \mathbb{Z}} \left| \int_{mh}^{mh+h} f\left(\begin{bmatrix} x_1 \\ nh \end{bmatrix}\right) dx_1 - \int_{mh}^{mh+h} \left(l_{mn}\left(\begin{bmatrix} x_1 \\ nh \end{bmatrix}\right) \right) dx_1 \right|. \end{aligned} \quad (47)$$

Since $\forall \|x\| \geq (p+1/2)h$, $\varphi(x) = 0$, there are only $p+1$ number of ms satisfying

$$\left| \int_{mh}^{mh+h} \left(f\left(\begin{bmatrix} x_1 \\ nh \end{bmatrix}\right) \right) dx_1 - \int_{mh}^{mh+h} \left(l_{mn}\left(\begin{bmatrix} x_1 \\ nh \end{bmatrix}\right) \right) dx_1 \right| \neq 0, \quad (48)$$

and all of them satisfy Eq. (46). Then, by Eqs. (46), (47) and (48), we can easily achieve (43).

2) We then prove

$$\begin{aligned} & \left| \int_{\mathbb{R}^2} f(x) d\sigma(x) - \sum_{n \in \mathbb{Z}} \int_{\mathbb{R}} f\left(\begin{bmatrix} x_1 \\ nh \end{bmatrix}\right) dx_1 h \right| \\ &\leq \frac{(p+1)^2 C}{8} h^4. \end{aligned} \quad (49)$$

Let $F(x_2) = \int_{\mathbb{R}} f\left(\begin{bmatrix} x_1 \\ x_2 \end{bmatrix}\right) dx_1$, and then

$$\int_{\mathbb{R}^2} f(x) d\sigma(x) = \int_{\mathbb{R}} F(x_2) dx_2. \quad (50)$$

By Lemma 1, we can obtain that $|F''(x_2)| \leq (p+1)hC$. Let $L_n(x_2)$ be the linear interpolation function of $F(x_2)$ between points $x_2 = nh$ and $x_2 = nh+h$. Then $\forall x_2 \in [nh, nh+h]$, by Lemma 2, we have

$$|F(x_2) - L_n(x_2)| \leq \frac{(p+1)C}{8} h^3. \quad (51)$$

Thus, similar to Eq. (46) we can deduce that

$$\begin{aligned} & \left| \int_{nh+h}^{nh} F(x_2) dx_2 - \int_{nh+h}^{nh} L_n(x_2) dx_2 \right| \\ &\leq \int_{nh+h}^{nh} |F(x_2) - L_n(x_2)| dx_2 \\ &\leq \frac{(p+1)C}{8} h^4. \end{aligned} \quad (52)$$

Besides, similar to Eq. (47) we can deduce that

$$\begin{aligned} & \left| \int_{\mathbb{R}^2} f(x) d\sigma(x) - \sum_{n \in \mathbb{Z}} \int_{\mathbb{R}} f\left(\begin{bmatrix} x_1 \\ nh \end{bmatrix}\right) dx_1 h \right| \\ &= \left| \int_{\mathbb{R}} F(x_2) dx_2 - \sum_{n \in \mathbb{Z}} F(nh) h \right| \\ &= \left| \int_{\mathbb{R}} F(x_2) dx_2 - \sum_{n \in \mathbb{Z}} \frac{1}{2}(F(nh) + F(nh+h)) h \right| \\ &\leq \sum_{n \in \mathbb{Z}} \left| \int_{nh}^{nh+h} F(x_2) dx_2 - \frac{1}{2}(F(nh) + F(nh+h)) h \right|. \end{aligned} \quad (53)$$

Since $\forall \|x\| \geq (p+1/2)h$, $\varphi(x) = 0$, there are only $p+1$ number of ms satisfying

$$\left| \int_{nh}^{nh+h} F(x_2) dx_2 - \frac{1}{2}(F(nh) + F(nh+h)) h \right| \neq 0, \quad (54)$$

and all of them satisfy (52). Then, by Eqs. (52), (53) and (54), we can easily achieve (49).

3) By Eqs. (43) and (49), we can obtain

$$\begin{aligned} & \left| \int_{\mathbb{R}^2} \varphi(\tilde{A}^{-1}x) r(y-x) d\sigma(x) - \sum_{i,j \in \Lambda} \varphi(\tilde{A}^{-1}x_{ij}) r(y-x_{ij}) h^2 \right| \\ &= \left| \int_{\mathbb{R}} f(x) dx - \sum_{m,n \in \mathbb{Z}} f\left(\begin{bmatrix} mh \\ nh \end{bmatrix}\right) h^2 \right| \\ &\leq \left| \int_{\mathbb{R}} f(x) dx - \sum_{n \in \mathbb{Z}} \int_{\mathbb{R}} f\left(\begin{bmatrix} x_1 \\ nh \end{bmatrix}\right) dx_1 h \right| + \\ &\quad \sum_{n \in \mathbb{Z}} \left| \int_{\mathbb{R}} f\left(\begin{bmatrix} x_1 \\ nh \end{bmatrix}\right) dx_1 - \sum_{m \in \mathbb{Z}} f\left(\begin{bmatrix} x_1 \\ nh \end{bmatrix}\right) h \right| h, \end{aligned}$$

where, by (49),

$$\begin{aligned} & \left| \int_{\mathbb{R}} f(x) dx - \sum_{n \in \mathbb{Z}} \int_{\mathbb{R}} f\left(\begin{bmatrix} x_1 \\ nh \end{bmatrix}\right) dx_1 h \right| \\ &\leq \frac{(p+1)^2 C}{8} h^4. \end{aligned} \quad (55)$$

Besides, Since $\forall \|x\| \geq (p+1/2)h$, $\varphi(x) = 0$, there are only $p+1$ number of ms satisfying

$$\left| \int_{\mathbb{R}} f\left(\begin{bmatrix} x_1 \\ nh \end{bmatrix}\right) dx_1 - \sum_{m \in \mathbb{Z}} f\left(\begin{bmatrix} x_1 \\ nh \end{bmatrix}\right) h \right| \neq 0, \quad (56)$$

Thus, by (43), we have

$$\begin{aligned} & \left| \sum_{n \in \mathbb{Z}} \left| \int_{\mathbb{R}} f\left(\begin{bmatrix} x_1 \\ nh \end{bmatrix}\right) dx_1 - \sum_{m \in \mathbb{Z}} f\left(\begin{bmatrix} x_1 \\ nh \end{bmatrix}\right) h \right| h \right| \\ &\leq \frac{(p+1)^2 C}{8} h^4. \end{aligned} \quad (57)$$

Combining Eqs. (55), (55), (56), we can then deduce (42), which completes the proof. \square

Finally, let us prove the following theorem.

Theorem 3. Assume that an image $I \in \mathbb{R}^{n \times n}$ is discretized from the smooth function $r : \mathbb{R}^2 \rightarrow \mathbb{R}$ by (22), a feature map $F \in \mathbb{R}^{n \times n \times t}$ is discretized from the smooth function $e : \mathbb{R}^2 \times S \rightarrow \mathbb{R}$ by (23), $|S| = t$, and filters $\tilde{\Psi}$, $\tilde{\Phi}$ and $\tilde{\Upsilon}$ are generated from φ_{in} , φ_{out} and φ_A , $\forall A \in S$, by (24), respectively. If for any $A \in S$, $x \in \mathbb{R}^2$, the following conditions are satisfied:

$$\begin{aligned} & |r(x)|, |e(x, A)| \leq F_1, \\ & \|\nabla r(x)\|, \|\nabla e(x, A)\| \leq G_1, \\ & \|\nabla^2 r(x)\|, \|\nabla^2 e(x, A)\| \leq H_1, \\ & |\varphi_{in}(x)|, |\varphi_A(x)|, |\varphi_{out}(x)| \leq F_2, \\ & \|\nabla \varphi_{in}(x)\|, \|\nabla \varphi_A(x)\|, \|\nabla \varphi_{out}(x)\| \leq G_2, \\ & \|\nabla^2 \varphi_{in}(x)\|, \|\nabla^2 \varphi_A(x)\|, \|\nabla^2 \varphi_{out}(x)\| \leq H_2, \\ & \forall \|x\| \geq (p+1)h/2, \varphi_{in}(x), \varphi_A(x), \varphi_{out}(x) = 0, \end{aligned} \quad (58)$$

where p is the filter size, h is the mesh size, ∇ and ∇^2 denote the operators of gradient and Hessian matrix, respectively. Then, for any $\tilde{A} \in S$, the following rules are satisfied:

$$\begin{aligned} & \|\tilde{\Psi} \star \tilde{\pi}_{\tilde{A}}^R(I) - \tilde{\pi}_{\tilde{A}}^{\tilde{E}}(\tilde{\Psi} \star I)\|_{\infty} \leq \frac{C}{2}(p+1)^2h^2, \\ & \|\tilde{\Phi} \star \tilde{\pi}_{\tilde{A}}^{\tilde{E}}(F) - \tilde{\pi}_{\tilde{A}}^{\tilde{E}}(\tilde{\Phi} \star F)\|_{\infty} \leq \frac{C}{2}(p+1)^2h^2t, \\ & \|\tilde{\Upsilon} \star \tilde{\pi}_{\tilde{A}}^{\tilde{E}}(F) - \tilde{\pi}_{\tilde{A}}^R(\tilde{\Upsilon} \star F)\|_{\infty} \leq \frac{C}{2}(p+1)^2h^2t, \end{aligned} \quad (59)$$

where $C = F_1H_2 + F_2H_1 + 2G_1G_2$, $\tilde{\pi}_{\tilde{A}}^R$, $\tilde{\pi}_{\tilde{A}}^{\tilde{E}}$, $\tilde{\Psi}$, $\tilde{\Phi}$ and $\tilde{\Upsilon}$ are defined in (24) and (29), the operator \star is defined in (26), (27) and (28), respectively, and $\|\cdot\|_{\infty}$ represents the infinity norm.

Proof. For any $y \in \mathbb{R}$, $A, B \in S$, let

$$\hat{\Psi}[r](y, A) = \sum_{(\tilde{i}, \tilde{j}) \in \Lambda} \varphi_{in}(A^{-1}x_{\tilde{i}\tilde{j}}) r(y - x_{\tilde{i}, \tilde{j}}), \quad (60)$$

where $\Lambda = \{(\tilde{i}, \tilde{j}) | \tilde{i}, \tilde{j} = 1, 2, \dots, p\}$. Then, for any $A \in S$ we can obtain

$$\hat{\Psi}[r](y_{ij}, A) = (\tilde{\Psi} \star I)_{ij}^A. \quad (61)$$

1) By Theorem 2, we know that $\Psi[\pi_{\tilde{A}}^R[r]] = \pi_{\tilde{A}}^E[\Psi[r]]$, and thus for any $A \in S$, it holds that

$$\begin{aligned} & \left| (\tilde{\Psi} \star \tilde{\pi}_{\tilde{A}}^R(I) - \tilde{\pi}_{\tilde{A}}^{\tilde{E}}(\tilde{\Psi} \star I))_{ij}^A \right| \\ &= \left| \hat{\Psi}[\pi_{\tilde{A}}^R[r]](y_{ij}, A) - \pi_{\tilde{A}}^E[\hat{\Psi}[r]](y_{ij}, A) \right| \\ &\leq \left| \hat{\Psi}[\pi_{\tilde{A}}^R[r]](y_{ij}, A) - \frac{1}{h^2} \Psi[\pi_{\tilde{A}}^R[r]](y_{ij}, A) \right| \\ &+ \left| \pi_{\tilde{A}}^E[\hat{\Psi}[r]](y_{ij}, A) - \frac{1}{h^2} \pi_{\tilde{A}}^E[\Psi[r]](y_{ij}, A) \right|. \end{aligned} \quad (62)$$

Let $\hat{r} = \pi_{\tilde{A}}^R[r]$, and then it is easy to deduce that \hat{r} satisfies the conditions in Lemma 3. Then, by Lemma 3, we have

$$\begin{aligned} & \left| \hat{\Psi}[\pi_{\tilde{A}}^R[r]](y_{ij}, A) - \frac{1}{h^2} \Psi[\pi_{\tilde{A}}^R[r]](y_{ij}, A) \right| \\ &= \frac{1}{h^2} \left| \hat{\Psi}[\pi_{\tilde{A}}^R[r]](y_{ij}, A)h^2 - \Psi[\pi_{\tilde{A}}^R[r]](y_{ij}, A) \right| \\ &= \frac{1}{h^2} \left| \sum_{(i,j) \in \Lambda} \varphi_{in}(A^{-1}x_{ij}) \hat{r}(y_{ij} - x_{i,j}) h^2 - \right. \\ & \quad \left. \int_{\mathbb{R}^2} \varphi_{in}(A^{-1}x) \hat{r}(y_{ij} - x) d\sigma(x) \right| \\ &\leq \frac{(p+1)^2 C}{4} h^2. \end{aligned} \quad (63)$$

Besides, let $\hat{A} = \tilde{A}^{-1}A$ and $\hat{y}_{ij} = \tilde{A}^{-1}y_{ij}$, and then by Lemma 3, we can also achieve

$$\begin{aligned} & \left| \pi_{\tilde{A}}^E[\hat{\Psi}[r]](y_{ij}, A) - \frac{1}{h^2} \pi_{\tilde{A}}^E[\Psi[r]](y_{ij}, A) \right| \\ &= \frac{1}{h^2} \left| \pi_{\tilde{A}}^E[\hat{\Psi}[r]](y_{ij}, A)h^2 - \pi_{\tilde{A}}^E[\Psi[r]](y_{ij}, A) \right| \\ &= \frac{1}{h^2} \left| \sum_{(i,j) \in \Lambda} \varphi_{in}(\hat{A}^{-1}x_{ij}) r(\hat{y}_{ij} - x_{i,j}) h^2 - \right. \\ & \quad \left. \int_{\mathbb{R}^2} \varphi_{in}(\hat{A}^{-1}x) r(\hat{y}_{ij} - x) d\sigma(x) \right| \\ &\leq \frac{(p+1)^2 C}{4} h^2. \end{aligned} \quad (64)$$

Thus, by combining (62), (63) and (64), we can achieve

$$\left| \hat{\Psi}[\pi_{\tilde{A}}^R[r]](y_{ij}, A) - \pi_{\tilde{A}}^E[\hat{\Psi}[r]](y_{ij}, A) \right| \leq \frac{C}{2}(p+1)^2h^2. \quad (65)$$

That is,

$$\left| (\tilde{\Psi} \star \tilde{\pi}_{\tilde{A}}^R(I) - \tilde{\pi}_{\tilde{A}}^{\tilde{E}}(\tilde{\Psi} \star I))_{ij}^A \right| \leq \frac{C}{2}(p+1)^2h^2. \quad (66)$$

The first inequality in (59) can then be proved.

2) For any $A, B \in S$, let $\hat{B} = \tilde{A}^{-1}B$, $r_A = e(x, A)$, and $\hat{\Psi}_A$ be an operator defined in the formulation of (60), while correlated to φ_A . Then, for any $i, j = 1, 2, \dots, n$, $B \in S$, it holds that

$$\begin{aligned} & \left| (\tilde{\Phi} \star \tilde{\pi}_{\tilde{A}}^{\tilde{E}}(F) - \tilde{\pi}_{\tilde{A}}^{\tilde{E}}(\tilde{\Phi} \star F))_{ij}^B \right| \\ &= \left| \sum_{(\tilde{i}, \tilde{j}) \in \Lambda, A \in S} \varphi_A(B^{-1}x_{\tilde{i}\tilde{j}}) e(\tilde{A}^{-1}(y_{ij} - x_{\tilde{i}, \tilde{j}}), \tilde{A}^{-1}BA) - \right. \\ & \quad \left. \sum_{(\tilde{i}, \tilde{j}) \in \Lambda, A \in S} \varphi_A(B^{-1}\tilde{A}x_{\tilde{i}\tilde{j}}) e(\tilde{A}^{-1}y_{ij} - x_{\tilde{i}, \tilde{j}}, \tilde{A}^{-1}BA) \right| \\ &\leq \sum_{A \in S} \left| \sum_{(\tilde{i}, \tilde{j}) \in \Lambda} \varphi_A(B^{-1}x_{\tilde{i}\tilde{j}}) r_{\hat{B}A}(\tilde{A}^{-1}y_{ij} - \tilde{A}^{-1}x_{\tilde{i}, \tilde{j}}) - \right. \\ & \quad \left. \sum_{(\tilde{i}, \tilde{j}) \in \Lambda} \varphi_A(B^{-1}\tilde{A}x_{\tilde{i}\tilde{j}}) r_{\hat{B}A}(\tilde{A}^{-1}y_{ij} - x_{\tilde{i}, \tilde{j}}) \right| \end{aligned}$$

$$\begin{aligned}
&= \sum_{A \in S} \left| \sum_{(\tilde{i}, \tilde{j}) \in \Lambda} \varphi_A \left(B^{-1} x_{\tilde{i}\tilde{j}} \right) \pi_A^R [r_{\hat{B}A}] \left(y_{ij} - x_{\tilde{i}, \tilde{j}} \right) - \right. \\
&\quad \left. \sum_{(\tilde{i}, \tilde{j}) \in \Lambda} \varphi_A \left(B^{-1} \tilde{A} x_{\tilde{i}\tilde{j}} \right) r_{\hat{B}A} \left(\tilde{A}^{-1} y_{ij} - x_{\tilde{i}, \tilde{j}} \right) \right| \\
&= \sum_{A \in S} \left| \hat{\Psi}_A \left[\pi_A^R [r_{\hat{B}A}] \right] (y_{ij}, B) - \pi_A^E \left[\hat{\Psi}_A [r_{\hat{B}A}] \right] (y_{ij}, B) \right|.
\end{aligned}$$

Then by Eq. (65), we can achieve that $\forall i, j = 1, 2, \dots, n$, $B \in S$,

$$\left| \left(\tilde{\Phi} \star \tilde{\pi}_{\tilde{A}}^E (F) - \pi_{\tilde{A}}^E (\tilde{\Phi} \star F) \right)_{ij}^B \right| \leq \frac{C}{2} (p+1)^2 h^2 t. \quad (67)$$

The second inequality in (59) is thus also proved.

3) For any $A, B \in S$, let $\hat{B} = \tilde{A}^{-1} B$, $r_A = e(x, A)$, and $\hat{\Psi}_{out}$ be an operator defined in the formulation of (60), while correlated to φ_{out} . Then, $\forall i, j = 1, 2, \dots, n$, it holds that

$$\begin{aligned}
&\left| \left(\tilde{\Upsilon} \star \tilde{\pi}_{\tilde{A}}^E (F) - \pi_{\tilde{A}}^E (\tilde{\Upsilon} \star F) \right)_{ij} \right| \\
&= \left| \sum_{(\tilde{i}, \tilde{j}) \in \Lambda, B \in S} \varphi_{out} \left(B^{-1} x_{\tilde{i}\tilde{j}} \right) e \left(\tilde{A}^{-1} \left(y_{ij} - x_{\tilde{i}, \tilde{j}} \right), \tilde{A}^{-1} B \right) - \right. \\
&\quad \left. \sum_{(\tilde{i}, \tilde{j}) \in \Lambda, B \in S} \varphi_{out} \left(B^{-1} \tilde{A} x_{\tilde{i}\tilde{j}} \right) e \left(\tilde{A}^{-1} y_{ij} - x_{\tilde{i}, \tilde{j}}, \tilde{A}^{-1} B \right) \right| \\
&\leq \sum_{B \in S} \left| \sum_{(\tilde{i}, \tilde{j}) \in \Lambda} \varphi_{out} \left(B^{-1} x_{\tilde{i}\tilde{j}} \right) r_{\hat{B}} \left(\tilde{A}^{-1} y_{ij} - \tilde{A}^{-1} x_{\tilde{i}, \tilde{j}} \right) - \right. \\
&\quad \left. \sum_{(\tilde{i}, \tilde{j}) \in \Lambda} \varphi_{out} \left(B^{-1} \tilde{A} x_{\tilde{i}\tilde{j}} \right) r_{\hat{B}} \left(\tilde{A}^{-1} y_{ij} - x_{\tilde{i}, \tilde{j}} \right) \right| \\
&= \sum_{B \in S} \left| \sum_{(\tilde{i}, \tilde{j}) \in \Lambda} \varphi_{out} \left(B^{-1} x_{\tilde{i}\tilde{j}} \right) \pi_{\tilde{A}}^R [r_{\hat{B}}] \left(y_{ij} - x_{\tilde{i}, \tilde{j}} \right) - \right. \\
&\quad \left. \sum_{(\tilde{i}, \tilde{j}) \in \Lambda} \varphi_{out} \left(B^{-1} \tilde{A} x_{\tilde{i}\tilde{j}} \right) r_{\hat{B}} \left(\tilde{A}^{-1} y_{ij} - x_{\tilde{i}, \tilde{j}} \right) \right| \\
&= \sum_{B \in S} \left| \hat{\Psi}_{out} \left[\pi_{\tilde{A}}^R [r_{\hat{B}}] \right] (y_{ij}, B) - \pi_{\tilde{A}}^E \left[\hat{\Psi}_{out} [r_{\hat{B}}] \right] (y_{ij}, B) \right|.
\end{aligned}$$

Then by (65), we can achieve that $\forall i, j = 1, 2, \dots, n$,

$$\left| \left(\tilde{\Upsilon} \star \tilde{\pi}_{\tilde{A}}^E (F) - \pi_{\tilde{A}}^E (\tilde{\Upsilon} \star F) \right)_{ij} \right| \leq \frac{C}{2} (p+1)^2 h^2 t. \quad (68)$$

The third inequality in (59) is then proved. \square

3 DETAILS OF SETTING $\Omega(x)$

In the definition of the proposed bases (2), we exploit a circular radial mask function $\Omega(x)$ to limit the range of bases, and make them more suitable for rotation. Specifically, we set it as:

$$\Omega(x) = \begin{cases} 0 & \text{if } \|x\| \geq r + h \\ \exp \left(-\frac{\|x\|^2 - r^2}{0.2 \cdot r^2} \right) & \text{if } r \leq \|x\| < r + h, \\ 1 & \text{if } \|x\| < r \end{cases} \quad (69)$$

where $r = (p-1/2)h$. It is easy to deduce that when $\|x\| < r$, $\Omega(x) = 1$, and the $\Omega(x)$ is in a circular shape with soft edge.

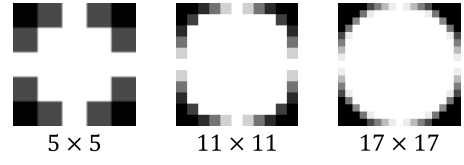


Fig. 1. Illustration of the circular radial mask function $\Omega(x)$. From left to right: the illustrations of $\Omega(x)$ discretized with filter sizes $p = 5$, $p = 11$ and $p = 17$, respectively.

Fig. 1 is an illustration of the exploited $\Omega(x)$, where we can see that when the filter size p is larger, the mask shows more elaborate circular shapes.

4 MORE EXPERIMENTAL RESULTS

In this section, we show more experimental results on the proposed bases for filter parametrization, including more intuitive basis demonstrations, more verifications of filter parametrization and more super-resolution experimental results.

4.1 Rotation of Bases

The capability of alleviating the fences phenomenon when being rotated to an arbitrary angle is the most important advantage of the proposed filter parametrization method, as compared to the conventional 2D Fourier series expansion. In Fig. 3 of the main text, we have shown the superiority of the proposed bases as compared to the traditional 2D Fourier bases, by an example of rotating a typical basis. Here, we show more examples to further demonstrate such superiority of proposed bases.

In Fig. 2, we show the rotation of all the proposed bases (φ_{kl}^c and φ_{kl}^s , $k, l = 1, 2, \dots, p-1$, defined in (2)), as compared to the traditional 2D Fourier bases (ϕ_{kl}^c and ϕ_{kl}^s , $k, l = 1, 2, \dots, p-1$, defined in (1)), where the patch size is $p = 11$. From Fig. 2(a), one can see that when being clock-wisely rotated with 45° , the high frequency ones of 2D Fourier bases suffered from heavy fences phenomenon, i.e., many of bases are largely degenerated into other shapes, which even results in an unexpected vortex-like pattern in the map of bases. Comparatively, As shown in Fig. 2(b), the proposed bases finely alleviate the fences phenomenon in most of the bases. Specifically, most of the bases are able to keep their original shapes when being rotated, and the vortex-like patterns no longer arise.

4.2 More Filter Parametrization Verifications

In this section, we will visually show more examples about the proposed filter parametrization method, with comparison to traditional 2D Fourier bases based (Fourier), the harmonics based (harmonic) [2], [4] and partial differential operator (PDO) based [1] filter parametrization strategies.

Figs. 3 and 4 show two examples of strip-pattern filters and their rotated ones by all competing methods. It can be easily observed that the proposed filter parametrization method can achieve results most close to the ground truth. Especially, in the 11×11 cases, the difference of the results represented by the proposed method is indistinguishable from the ground truth by intuition. As comparison, the

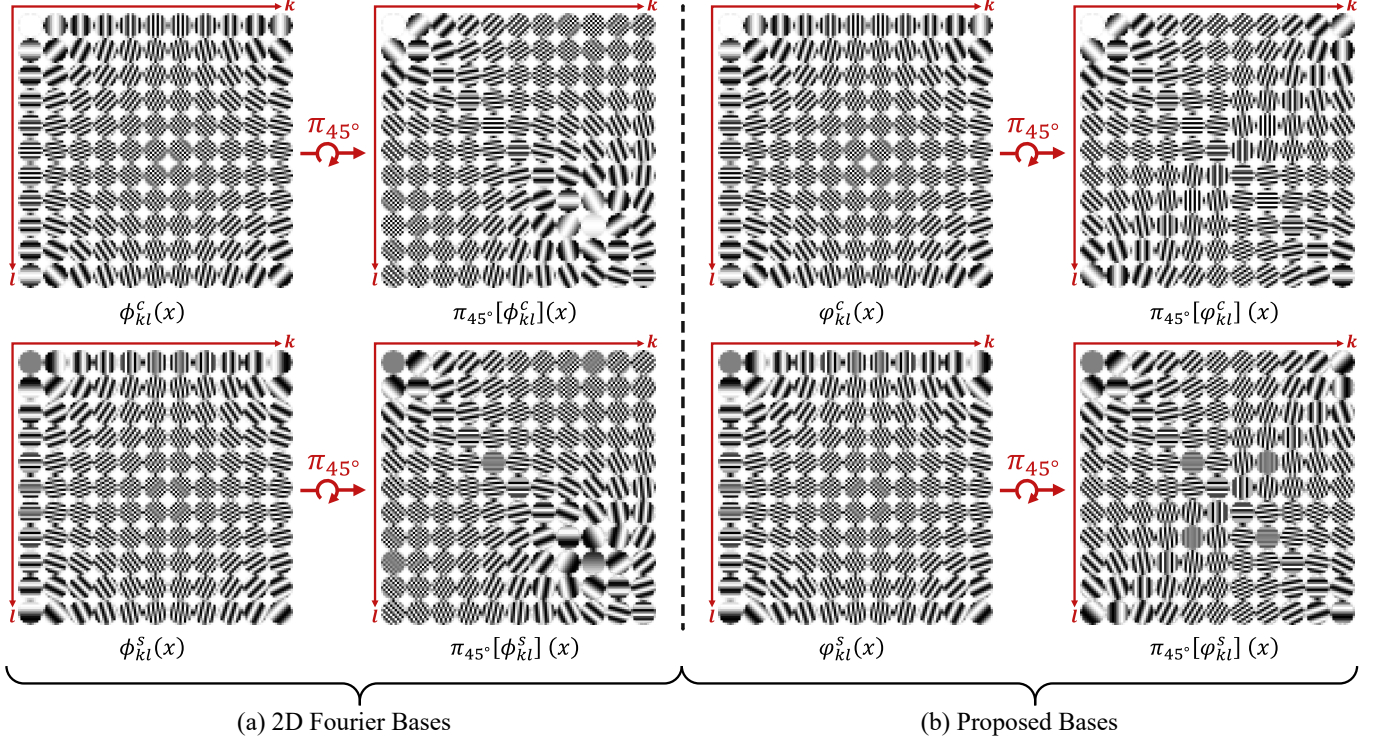


Fig. 2. (a) Illustrations of the 2D Fourier bases, ϕ_{kl}^c and ϕ_{kl}^s , and their 45° rotations (rotated by $\pi_{45^\circ}(\cdot)$), where $k, l = 0, 1, \dots, p - 1$ and $p = 11$. The heavy fences phenomenon can be easily observed in many of the bases, which also results in unexpected vortex-like patterns in the map of these bases. (b) Illustrations of the proposed bases, φ_{kl}^c and φ_{kl}^s , and their 45° rotations, where $k, l = 0, 1, \dots, p - 1$ and $p = 11$. The fences phenomenon is obviously alleviated.

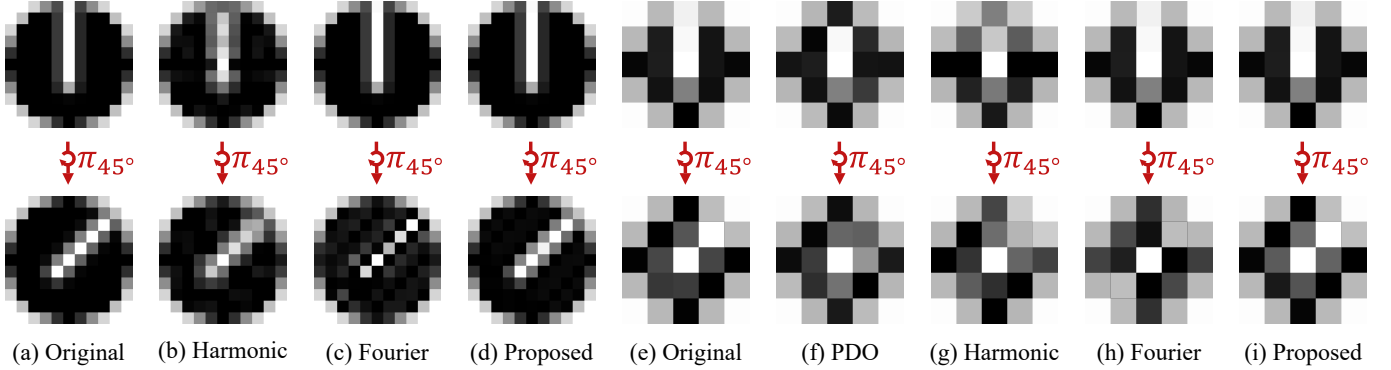


Fig. 3. (a) A discretization of a strip-pattern functional filter and its $\pi/4$ rotation, with filter size $p = 11$ and mesh size $h = 1/5$. (b)-(d) The representations and corresponding $\pi/4$ rotations of a given 2D filter obtained by adopting the harmonics bases [2], the 2D Fourier bases [3] and the proposed bases as representing basis functions, respectively. (e) A discretization of the same strip-pattern functional filter, with filter size $p = 5$ and mesh size $h = 1/2$. (f)-(i) The representations and corresponding $\pi/4$ rotations of a given 2D filter, obtained by employing the PDO bases [1], the harmonics bases [2], 2D Fourier bases [3] and the proposed bases as the representing basis functions, respectively.

Harmonic based parametrization method achieves over smooth results. Moreover, there are unexpected ring-shape artifacts existed in the results of this method, as can be easily observed in Fig. 3, where the strip-pattern is thin. This might possibly be due to the ring-shape radial parts in Harmonic based parametrization. The commonly used Fourier bases can achieve an accurate parametrization result (the same as the proposed method). However, its rotation results show unsatisfactory configurations, especially in Fig. 4, where the strip-pattern is thick. The PDO based method can be only used when the filter size is 5×5 , and the representing/rotating results also contain certain degree of

quality degradation.

4.3 More Super-resolution Experimental Results

In the main text, we have adopted the filter parameterized equivariant convolutions to a typical low-level image processing task, image super-resolution (SR), for verifying their performance. In this section, we will show more experimental results in details.

The experimental setting here is completely the same as that introduced in the main text, where we exploit 3 state-of-the-art networks designed for SR tasks, i.e., EDSR [5], RDN [6] and RCAN [7] for our experiments. The competing

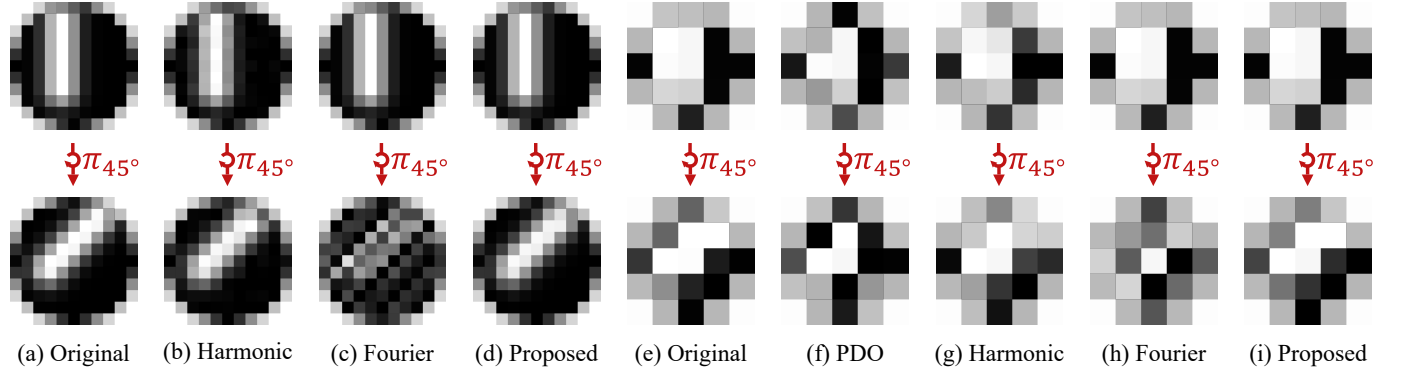


Fig. 4. (a) A discretization of a strip-pattern functional filter and its $\pi/4$ rotation, with filter size $p = 11$, mesh size $h = 1/5$. (b)-(d) The representations and correlated $\pi/4$ rotations of a given 2D filter, where we adopt harmonics bases [2], 2D Fourier bases [3] and the proposed bases as basis functions, respectively. (e) A discretization of the same functional filter, with filter size $p = 5$, mesh size $h = 1/2$. (f)-(i) The representations and correlated $\pi/4$ rotations of a given 2D filter, by adopting PDO bases [1], harmonics bases [2], 2D Fourier bases [3] and the proposed bases as basis functions, respectively.

equivariant convolution methods include G-CNN [8], E2-CNN [4], PDO-eConv [1] and the proposed F-Conv. We replace the original convolutions in EDSR, RDN and RCAN with the competing convolutions, respectively, and compare their performance.

We have carefully set the channel and transformation group sizes of equivariant convolutions, to guarantee the network architectures based on different convolutions possessing similar memories. For G-CNN based network, since an intermediate feature map is a 4-channel matrix, we set the channel number of residual blocks as $1/4$ of that in the original networks, so as to make it have the similar memory as the original network. Following the original setting in EDSR, RDN and RCAN, the filter size is set as 3×3 in G-CNN based network. For E2-CNN, PDO-eConv and the proposed F-Conv, we exploit $p8$ group for the equivariant convolutions and set the channel number of each residual block (and the growth rate in RDN) as $1/8$ to the original networks in each layer to make them take similar amount of memory as the original network. Besides, we set the filter size as 5×5 for these convolutions (due to the fact that the PDO-eConv is only designed for filters with size 5×5 , and the circular shape mask in filters of E2CNN and F-Conv make 3×3 filters contain too few effective pixels). Since the channel attention operation is not rotation equivariant, we remove the channel attention modular in the equivariant-convolution-based RCAN methods. It should be noted that in these equivariant-convolution-based SR methods, the entire architecture of these networks are almost rotation equivariant, and only the upsampling operators at the tail parts of the networks are not rotation equivariant.

Following [5], [6], [7], we use 800 training images from DIV2K dataset [9] as the training set. For testing, we use five standard benchmark datasets, Urban100 [10], B100 [11], Set14 [12] and Set5 [13], which contain 100, 100, 14 and 5 natural images, respectively. We conduct experiments with Bicubic (BI) and degradation models [5], [6], [7]. We use Adam optimizer [14] with no weight decay to train the networks for 150 epoches. We first train the competing methods without data augmentation, in order to observe the benefit effects from equivariant convolutions. Then, following the setting of previous methods, we also train the competing

methods with randomly rotated training images by 90° , 180° , 270° and flipping horizontally for data augmentation.

Quantitative results. Tables 1 and 2 show the SR results of all competing methods on the 5 exploited data sets, without and with data augmentation, respectively. The evaluation measures include PSNR and SSIM [15] on the Y channel (i.e., luminance) of the transformed YCbCr space. Comparing the results in Tables 1 and 2, it is easy to observe that removing data augmentation will significantly affect the performance of the 3 CNN-based SR methods, especially in the 4 scale SR experiments. As comparison, the performance of equivariant-convolution-based methods does not change too much with or without data augmentation, since most of the network modulars in these methods are rotation equivariant. This implies that the rotation symmetries of local features and rotation equivariant convolutions do be helpful for improving SR performance. Besides, we can also observe that E2-CNN and PDO-eConv methods attain relatively unsatisfactory SR performance, which should be due to their limitation in the accuracy of the filter parametrization methods in these two method. Comparatively, the proposed F-Conv method evidently outperforms the other two filter-parametrization-based equivariant convolutions in this task and achieves better result than CNN and G-CNN based methods which don't involve filter parametrization.

Visual results. Fig. 5 and 6 visually compare the SR results obtained all competing methods on 2 samples from the B100 dataset, with SR scale respectively set as 2 and 4, trained with data augmentation. Fig. 7 and 8 visually show the SR results of all comparison methods on 2 samples from the Set14 dataset, with SR scale respectively set as 2 and 4, trained with data augmentation. From these figures, it is easy to observe that the SR results of filter parametrization based methods, like E2-CNN and PDO-eConv based methods, are mostly over smooth and lack of detail textures. As comparison, F-Conv based method performs relatively better in achieving clearer SR image and avoiding mistakenly restored textures, superior to the methods based on other 4 convolutions. These results substantiate that the proposed filter parametrization method shows more superiority for low-level computer vision tasks beyond the previous Harmonic and PDO based filter parametrization strategies.

TABLE 1

The average testing results of all competing method on 4 typical image datasets, including Urban100 [10], B100 [11], Set14 [12] and Set5 [13], where all models are trained without data argumentation.

Method	×2						×4					
	EDSR [5]		RDN [6]		RCAN [7]		EDSR [5]		RDN [6]		RCAN [7]	
	PNSR	SSIM										
Testing data: Urban100												
CNN	32.131	0.9296	32.135	0.9296	32.317	0.9315	25.927	0.7851	26.065	0.7891	26.042	0.7882
G-CNN [8]	32.222	0.9304	32.237	0.9303	32.457	0.9321	26.014	0.7867	26.087	0.7905	26.203	0.7937
E2-CNN [4]	31.867	0.9275	32.051	0.9289	31.516	0.9236	25.901	0.7831	26.023	0.7867	25.544	0.7719
PDO-eConv [1]	30.884	0.9156	30.544	0.9118	31.157	0.9189	25.327	0.7598	24.287	0.7196	25.321	0.7615
F-Conv	32.345	0.9312	32.514	0.9332	32.682	0.9343	26.243	0.7948	26.324	0.7968	26.321	0.7952
Testing data: B100												
CNN	32.191	0.9028	32.178	0.9207	32.212	0.9031	27.501	0.7432	27.564	0.7444	27.533	0.7438
G-CNN [8]	32.212	0.9031	32.213	0.9032	32.240	0.9034	27.561	0.7435	27.594	0.7453	27.600	0.7454
E2-CNN [4]	32.129	0.9023	32.158	0.9024	32.027	0.9010	27.529	0.7430	27.576	0.7435	27.415	0.7391
PDO-eConv [1]	31.848	0.8983	31.744	0.8972	31.921	0.8993	27.297	0.7343	26.815	0.7202	27.302	0.7352
F-Conv	32.221	0.9031	32.256	0.9306	32.302	0.9041	27.592	0.7454	27.631	0.7462	27.638	0.7455
Testing data: Set14												
CNN	33.637	0.9195	33.593	0.9196	33.585	0.9202	28.452	0.7853	28.546	0.7875	28.539	0.7864
G-CNN [8]	33.630	0.9203	33.660	0.9203	33.688	0.9205	28.576	0.7867	28.648	0.7897	28.621	0.7890
E2-CNN [4]	33.545	0.9198	33.550	0.9190	33.334	0.9179	28.491	0.7857	28.576	0.7866	28.340	0.7809
PDO-eConv [1]	33.158	0.9161	32.998	0.9149	33.262	0.9169	28.235	0.7779	27.350	0.7575	28.200	0.7778
F-Conv	33.746	0.9207	33.769	0.9221	33.852	0.9215	28.579	0.7882	28.666	0.7898	28.651	0.7886
Testing data: Set5												
CNN	38.011	0.9621	38.046	0.9621	38.050	0.9622	32.135	0.8972	32.201	0.8981	32.196	0.8981
G-CNN [8]	37.998	0.9619	38.050	0.9622	38.087	0.9624	32.006	0.8961	32.165	0.8982	32.239	0.8985
E2-CNN [4]	37.921	0.9618	37.961	0.9619	37.780	0.9613	32.039	0.8957	32.106	0.8964	31.736	0.8917
PDO-eConv [1]	37.581	0.9605	37.443	0.9599	37.675	0.9608	31.589	0.8895	30.292	0.8617	31.584	0.8889
F-Conv	38.061	0.9623	38.103	0.9624	38.169	0.9625	32.259	0.8986	32.317	0.8995	32.295	0.8989

TABLE 2

The average testing results of all competing method on 4 typical image datasets, including Urban100 [10], B100 [11], Set14 [12] and Set5 [13], where all models are trained with data argumentation.

Method	×2						×4					
	EDSR [5]		RDN [6]		RCAN [7]		EDSR [5]		RDN [6]		RCAN [7]	
	PNSR	SSIM										
Testing data: Urban100												
CNN	32.220	0.9302	32.230	0.9303	32.359	0.9316	26.250	0.7935	26.303	0.7956	26.395	0.7979
G-CNN [8]	32.269	0.9306	32.237	0.9304	32.431	0.9320	26.264	0.7951	26.110	0.7912	26.316	0.7955
E2-CNN [4]	31.992	0.9283	32.095	0.9294	31.550	0.9238	25.898	0.7829	26.060	0.7885	25.626	0.7737
PDO-eConv [1]	30.912	0.9159	29.550	0.8994	31.082	0.9181	25.377	0.7617	24.370	0.7229	25.268	0.7597
F-Conv	32.357	0.9313	32.587	0.9340	32.747	0.9350	26.398	0.7982	26.416	0.7990	26.497	0.8010
Testing data: B100												
CNN	32.211	0.9032	32.215	0.9031	32.240	0.9034	27.641	0.7461	27.638	0.7461	27.667	0.7467
G-CNN [8]	32.209	0.9027	32.217	0.9032	32.261	0.9037	27.629	0.7460	27.610	0.7461	27.638	0.7461
E2-CNN [4]	32.148	0.9024	32.178	0.9028	32.035	0.9009	27.541	0.7429	27.585	0.7442	27.436	0.7396
PDO-eConv [1]	31.871	0.8985	31.429	0.8933	31.916	0.8994	27.322	0.7352	26.847	0.7214	27.273	0.7346
F-Conv	32.239	0.9034	32.290	0.9041	32.299	0.9042	27.650	0.7466	27.659	0.7469	27.690	0.7480
Testing data: Set14												
CNN	33.632	0.9199	33.630	0.9204	33.703	0.9202	28.673	0.7894	28.681	0.7904	28.722	0.7904
G-CNN [8]	33.606	0.9197	33.678	0.9204	33.747	0.9208	28.694	0.7901	28.658	0.7895	28.661	0.7893
E2-CNN [4]	33.513	0.9191	33.565	0.9200	33.361	0.9178	28.490	0.7853	28.610	0.7874	28.368	0.7811
PDO-eConv [1]	33.169	0.9161	32.511	0.9103	33.178	0.9163	28.241	0.7783	27.422	0.7590	28.171	0.7772
F-Conv	33.698	0.9205	33.832	0.9222	33.762	0.9213	28.715	0.7903	28.706	0.7904	28.743	0.7910
Testing data: Set5												
CNN	38.059	0.9621	38.066	0.9623	38.088	0.9623	32.314	0.8993	32.235	0.8989	32.331	0.8998
G-CNN [8]	38.041	0.9621	38.050	0.9623	38.119	0.9624	32.271	0.8991	32.170	0.8986	32.279	0.8991
E2-CNN [4]	37.912	0.9618	37.964	0.9620	37.789	0.9613	31.999	0.8953	32.085	0.8965	31.761	0.8920
PDO-eConv [1]	37.631	0.9606	36.824	0.9556	37.680	0.9608	31.606	0.8996	30.417	0.8641	31.460	0.8874
F-Conv	38.061	0.9622	38.136	0.9625	38.141	0.9624	32.316	0.8993	32.315	0.8997	32.386	0.9001

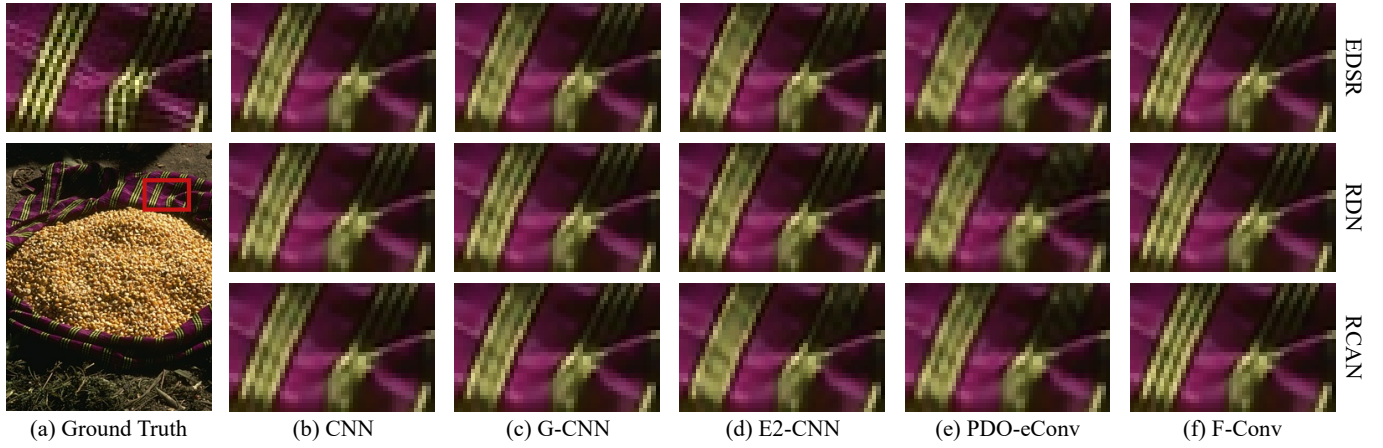


Fig. 5. (a) A sample of high-resolution image from the B100 [11] dataset. (b) From upper to lower: the 4 times super-resolution images restored by the EDSR, RDN and RCAN methods, respectively, where the convolution operator is set as commonly used convolution, i.e., CNN. (c)-(f) From upper to lower: the super-resolution images restored by the EDSR, RDN and RCAN methods, where the convolution operators are set as G-CNN, E2-CNN, PDO-eConv and the proposed F-Conv, respectively. All involved methods are trained with data argumentation.

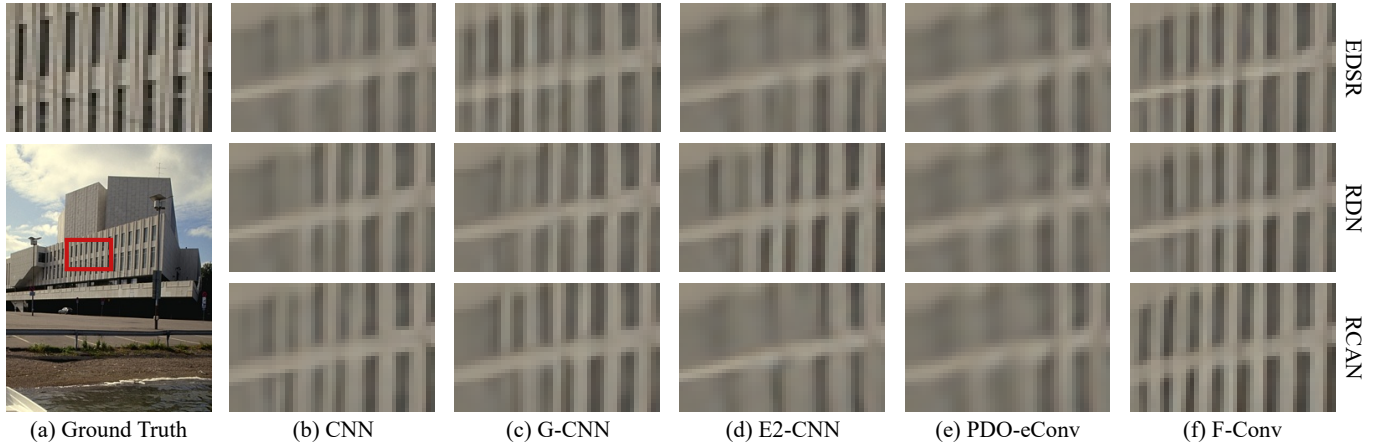


Fig. 6. (a) A sample of high-resolution image from the B100 [11] dataset. (b) From upper to lower: the 4 times super-resolution images restored by the EDSR, RDN and RCAN methods, respectively, where the convolution operator is set as commonly used convolution, i.e., CNN. (c)-(f) From upper to lower: the super-resolution images restored by the EDSR, RDN and RCAN methods, where the convolution operators are set as G-CNN, E2-CNN, PDO-eConv and the proposed F-Conv, respectively. All involved methods are trained with data argumentation.

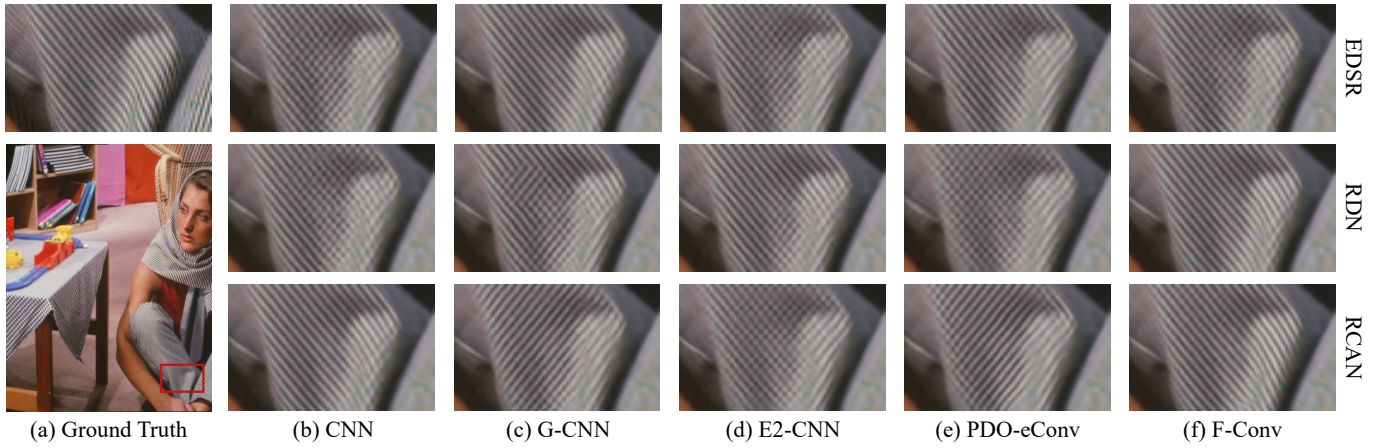


Fig. 7. (a) A sample of high-resolution image from the Set14 [12] dataset. (b) From upper to lower: the 4 times super-resolution images restored by the EDSR, RDN and RCAN methods, respectively, where the convolution operator is set as commonly used convolution, i.e., CNN. (c)-(f) From upper to lower: the super-resolution images restored by the EDSR, RDN and RCAN methods, where the convolution operators are set as G-CNN, E2-CNN, PDO-eConv and the proposed F-Conv, respectively. All involved methods are trained with data argumentation.

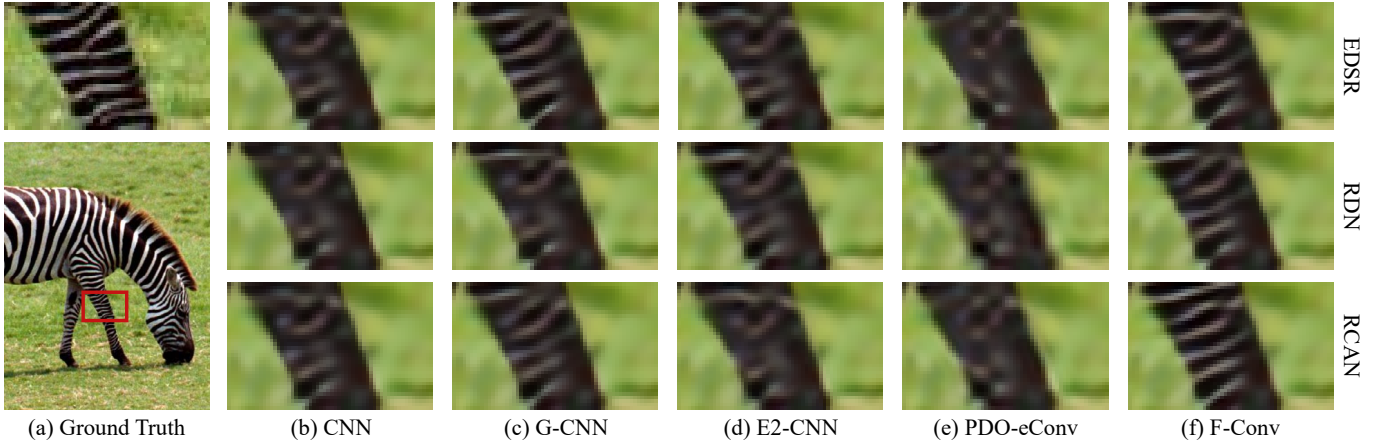


Fig. 8. (a) A sample of high-resolution image from the Set14 [12] dataset. (b) From upper to lower: the 4 times super-resolution images restored by the EDSR, RDN and RCAN methods, respectively, where the convolution operator is set as commonly used convolution, i.e., CNN. (c)-(f) From upper to lower: the super-resolution images restored by the EDSR, RDN and RCAN methods, where the convolution operators are set as G-CNN, E2-CNN, PDO-eConv and the proposed F-Conv, respectively. All involved methods are trained with data augmentation.

REFERENCES

- [1] Zhengyang Shen, Lingshen He, Zhouchen Lin, and Jinwen Ma. Pdo-econvs: Partial differential operator based equivariant convolutions. In *International Conference on Machine Learning*, pages 8697–8706. PMLR, 2020.
- [2] Maurice Weiler, Fred A Hamprecht, and Martin Storath. Learning steerable filters for rotation equivariant cnns. In *Proceedings of the IEEE Conference on Computer Vision and Pattern Recognition*, pages 849–858, 2018.
- [3] Soo-Chang Pei and Min-Hung Yeh. Two dimensional discrete fractional fourier transform. *Signal Processing*, 67(1):99–108, 1998.
- [4] Maurice Weiler and Gabriele Cesa. General $e(2)$ -equivariant steerable cnns. 2019.
- [5] Bee Lim, Sanghyun Son, Heewon Kim, Seungjun Nah, and Kyoung Mu Lee. Enhanced deep residual networks for single image super-resolution. In *Proceedings of the IEEE conference on computer vision and pattern recognition workshops*, pages 136–144, 2017.
- [6] Yulun Zhang, Yapeng Tian, Yu Kong, Bineng Zhong, and Yun Fu. Residual dense network for image super-resolution. In *Proceedings of the IEEE conference on computer vision and pattern recognition*, pages 2472–2481, 2018.
- [7] Yulun Zhang, Kunpeng Li, Kai Li, Lichen Wang, Bineng Zhong, and Yun Fu. Image super-resolution using very deep residual channel attention networks. In *Proceedings of the European conference on computer vision (ECCV)*, pages 286–301, 2018.
- [14] Jimmy Ba Diederik Kingma. Adam: A method for stochastic optimization. In *ICLR*, 2015.
- [8] Taco Cohen and Max Welling. Group equivariant convolutional networks. In *Proceedings of The 33rd International Conference on Machine Learning*, pages 2990–2999. PMLR, 2016.
- [9] Radu Timofte, Eirikur Agustsson, Luc Van Gool, Ming-Hsuan Yang, and Lei Zhang. Ntire 2017 challenge on single image super-resolution: Methods and results. In *Proceedings of the IEEE conference on computer vision and pattern recognition workshops*, pages 114–125, 2017.
- [10] Jia-Bin Huang, Abhishek Singh, and Narendra Ahuja. Single image super-resolution from transformed self-exemplars. In *Proceedings of the IEEE conference on computer vision and pattern recognition*, pages 5197–5206, 2015.
- [11] David Martin, Charless Fowlkes, Doron Tal, and Jitendra Malik. A database of human segmented natural images and its application to evaluating segmentation algorithms and measuring ecological statistics. In *Proceedings Eighth IEEE International Conference on Computer Vision. ICCV 2001*, volume 2, pages 416–423. IEEE, 2001.
- [12] Roman Zeyde, Michael Elad, and Matan Protter. On single image scale-up using sparse-representations. In *International conference on curves and surfaces*, pages 711–730. Springer, 2010.
- [13] Marco Bevilacqua, Aline Roumy, Christine Guillemot, and Marie Line Alberi-Morel. Low-complexity single-image super-resolution based on nonnegative neighbor embedding. 2012.
- [15] Zhou Wang, Alan C Bovik, Hamid R Sheikh, and Eero P Simoncelli. Image quality assessment: from error visibility to structural similarity. *IEEE transactions on image processing*, 13(4):600–612, 2004.